Detecting phase transitions in lattice gauge theories: Production and dissolution of topological defects in 4D compact electrodynamics

Loris Di Cairano,* Matteo Gori, Matthieu Sarkis, and Alexandre Tkatchenko

Department of Physics and Materials Science, University of Luxembourg, L-1511 Luxembourg City, Luxembourg

(Received 8 March 2023; revised 6 May 2024; accepted 16 May 2024; published 9 July 2024)

We present the application of microcanonical inflection point analysis (MIPA)—a novel and powerful method for the systematic identification and classification of phase transitions (PTs)—to the microcanonical formulation of lattice gauge theories. Specifically, we explore how this approach sheds light on collective phenomena such as the emergence of topological order in quantum field theories. As a case study, we show how to systematically characterize PTs in 4D $U(1)$ lattice electrodynamics. Beyond identifying the well-established deconfinement PT (DPT) associated with pair dissolution, classified as a first-order PT, we uncover two higher-order PTs not observed before. Thanks to the application of the MIPA, we identify an independent third-order PT in the confined phase and indications of a dependent third-order PT in the deconfined (Coulomb) phase. To gain physical insights into these PTs, we numerically compute the average number density of monopolar and pair defects as a function of energy. Notably, our findings reveal that the pair dissolution mechanism extends beyond a singular transitional phenomenon coinciding with the DPT. Instead, it encompasses a spectrum of transitional phenomena, as indicated by the rates of acceleration and deceleration in the dissolution of pairs as a function of energy. Finally, we briefly discuss how such a method can be extended to more complex quantum field theories on a lattice.

DOI: 10.1103/PhysRevD.110.014503

Phase transitions (PTs) are physical phenomena which involve abrupt and drastic changes in the phase of the system. They are usually accompanied by the emergence of collective phenomena, namely, by peculiar behaviors that emerge from the interactions of individual system's constituents, where the whole exhibits properties and dynamics not present in the individual components. PTs are omnipresent in nature, from protein folding in biology to the formation of stars in astrophysics, or from the superconducting PT in solid state physics to the generation of masses for the weak gauge bosons and fermions known as the Anderson-Higgs-Kibble mechanism [1–3] in quantum field theory. In the investigation of transitional phenomena, two questions are fundamental: (a) how to identify and characterize PTs in a given statistical ensemble based on a precise mathematical definition and (b) how to understand the deep physical origin, i.e., the mechanism for which the microscopic degrees of freedom interact giving rise to the macroscopic collective behavior. Focusing on the first question, the commonly accepted characterization of PTs is based on the (grand)canonical ensemble exploiting the Lee-Yang theorem [4,5] which states that PTs necessarily correspond to nonanalyticities of thermodynamic observables and they can only appear in the thermodynamic limit. The Lee-Yang theorem has then established a paradigm, PT = nonanalyticity = thermodynamic limit, that is implicitly assumed to hold for any other statistical ensemble. The presumed universal character of the Lee-Yang paradigm is strongly based on the necessity of invoking the thermodynamic limit since, in this limit, one expects the equivalence of ensembles [6], i.e., that all the ensembles provide the same physical information, no matter about the nature of microscopic interactions and of the undergoing PTs. Therefore, the choice of the ensemble is usually considered arbitrary, and any transitional phenomenon observed before taking the thermodynamic limit—which cannot manifest any discontinuity according with the Lee-Yang theorem–has been regarded as the signal of a (fictitious) finite-size effect rather than an *eventual* physical process. The first results that have questioned the alleged universality of the Lee-Yang paradigm have been provided by Ellis, Touchette *et al.* They have shown that (i) the equivalence of the ensembles is lost when a first-order PT occurs [7–10] and, as a consequence of that, (ii) the microcanonical ensemble is more fundamental than the canonical one, since, if we are in the presence of the nonequivalence of ensembles, the microcanonical observables can be always defined while the canonical ones may

*Corresponding author: loris.dicairano@uni.lu

suffer some mathematical pathologies [9]. See Appendix H for a brief discussion. On the other hand, substantial efforts have been made to understand how PTs manifest in the microcanonical ensemble. Gross proposed the *microcanonical analysis* [11,12] that has then been extended by Bachmann *et al.*, who developed a novel classification of PTs in the microcanonical ensemble called *microcanonical inflection point analysis* (MIPA) [13–22]. The application of MIPA to the 2D Ising model has provided remarkable results: new higher than second-order PTs have been discovered. These PTs appear at finite size, but survive in the thermodynamic limit and, in such a limit, do not manifest any catastrophic behavior [16,23]. Moreover, MIPA has also proven to be a powerful method for the classical lattice field theories [24–26] and for polymers [15,20,27]. Thus, the choice of the statistical ensemble is not *always* arbitrary for the purpose of identifying and classifying PTs. Moreover, in contrast to the Lee-Yang paradigm, PTs do not necessarily imply the presence of nonanalytic behaviors of the thermodynamic potentials, and they can already emerge at finite size. Phase transitions identified and classified through MIPA in finite-size systems are not guaranteed to persist in the thermodynamic limit whenever such a limit is relevant and well defined. However, MIPA is not limited to finite-size systems but can be applied to systems of *any* size, even including infinite size systems, as its effectiveness in detecting PTs is *independent of the system size*. For numerically investigated systems, the persistence of microcanonical PTs in the thermodynamic limit can be inferred through extrapolation from large but finite system sizes. Within the MIPA conceptual framework, this is achieved by verifying the persistence of inflection points in the derivatives of entropy as the system size increases. Therefore MIPA not only accommodates the concept of phase transition in finite-size systems, but also provides a classification scheme of PTs in the thermodynamic limit that is able to detect both the already known PTs and new PTs that have not been identified using the standard classification of PTs based on the appearance of nonanalytic behaviors in the thermodynamic potentials. Furthermore, it is crucial to emphasize that the PTs identified by MIPA effectively reflect qualitative and relevant changes in the collective behavior of microscopic degrees of freedom in response to slight variations in the control parameter, as shown in the 2D Ising model [23] and in the current work. Regarding the second original question, several mechanisms have been proposed for explaining the deep origin of PTs; however, a complete and unified theory of the origin of PTs has not been reached yet. In this respect, Landau suggested that the occurrence of PTs is triggered by a spontaneous symmetry breaking (SSB) mechanism [28,29] which is at the core of many PTs since it manifests not only in case of continuous symmetries such as the above-mentioned Higgs mechanism or the condensation mechanism of the Nambu-Goldstone bosons in condensed matter [30,31] but even for discrete symmetries such as for instance, the Z_N center symmetry in pure $SU(N)$ Yang-Mills theories [32,33]. In spite of its success, Landau's mechanism is not all encompassing since PTs can emerge also in the absence of a SSB as rigorously proved by Mermin and Wagner [34,35] and by Elitzur [36]. The Berezinskii-Kosterlitz-Thouless (BKT) PT provides the most emblematic example [37–39] observed in the 2D XY model where the transition is triggered by the emergence of topological defects, the vortices, that combine forming pairs of opposite "charge" called vortex-antivortex pairs whose dissociation causes the BKT PT. Another pair-dissolution mechanism that involves topological defects known as magnetic monopoles [40–46] is observed in Abelian lattice gauge theories (LGTs) as shown by Banks *et al.* [40–45,47] and gives rise to the so-called deconfinement PT (DPT). Of course, the emergence of topological defects, not being a peculiarity of systems with a nonbroken symmetry, can also be observed in those systems where the symmetry is broken [48,49]. Moreover, other classes of topological defects can be found in nature, such as skyrmions [50,51], cosmic domain and string in cosmology [52], wall domains in spin systems [53], and in liquid crystals [54].

In this paper, motivated by the considerations mentioned above, we investigate the transitional phenomena occurring in (compact) electrodynamics 4D $U(1)$ on a lattice combining the microcanonical formalism developed by Callaway [55–61] with MIPA. Besides the identification of the DPT, classified by MIPA as a first-order PT in agreement with the literature [43,44,62–66], our analysis reveals the presence of a novel (independent) third-order PT in the confined phase whereas, in the deconfined (Coulomb) phase, we have indications of the emergence of a (dependent) third-order PT. We then try to shed light on the deep origin/mechanism leading to these transitions studying the behaviors of topological defects, namely, the density of isolated monopoles and monopole-antimonopole pairs as functions of energy.

Let us consider an Abelian gauge field $A_\mu(\boldsymbol{x})$ discretized over a $d = 4$ dimensional Euclidean lattice with N sites per side and a lattice spacing a, so that the configuration degrees of freedom are $\phi_{\boldsymbol{n},\mu} \coloneqq a g_0 A_{\boldsymbol{n},\mu} \in [-\pi, \pi]$ where g_0 is the bare coupling constant. Each field variable $\phi_{\boldsymbol{n},\mu}$ is related to the link connecting the lattice point $\boldsymbol{n} \in [1, N]^4$ to its nearest neighbor in the space-time direction μ, i.e., $\boldsymbol{n} + \mu$. We employ the gauge-invariant Euclidean Wilson's action [67],

$$\mathcal{S}_W(\boldsymbol{\phi}) \coloneqq g_0^{-2} \sum_{\square} \left[1 - \cos\left(\Theta_{\mu\nu}(\boldsymbol{n})\right)\right], \tag{1}$$

where $\hbar = 1$, the sum is over the lattice plaquettes, $\square = \{\boldsymbol{n}, \mu, \nu\}$, uniquely identified by a site and two independent directions on the lattice. Then, $\Theta_{\mu\nu}(\boldsymbol{n}) \coloneqq \phi_{\boldsymbol{n},\mu} + \phi_{n+\mu,\nu} - \phi_{n+\nu,\mu} - \phi_{n,\nu}$ is the plaquette angle (see Appendix A). The microcanonical formulation of an Abelian LGT proposed by Callaway [55–57] consists of adding a kinetic term $K(\pi) = \sum_{n,\mu} \pi_{n,\mu}^2/2$ to the Wilson's

action (1) after the introduction of the fictitious momenta, $\pi_{n,\mu}$, conjugated to $\phi_{n,\mu}$. This manipulation does not alter the expectation value of quantum observables, but allows one to associate a dynamical system to any LGT whose Hamiltonian function is given by $\mathcal{H}(\pi,\phi) \coloneqq K(\boldsymbol{\pi}) + g_0^2 \mathcal{S}_W(\boldsymbol{\phi})$. Therefore, being the energy, E, fixed and conserved, we can naturally define the microcanonical ensemble introducing the microcanonical probability measure $d\rho \coloneqq \Omega_{N_{\rm ind}}^{-1}(E)\delta(\mathcal{H}[\pi,\phi]-E)\delta(\mathcal{C}(\pi))D\pi D\phi$, where, $\Omega_{N_{\rm ind}}(E) \coloneqq \int \delta(\mathcal{H}[\pi,\phi]-E)\delta(\mathcal{C}(\pi))D\pi D\phi$, is the microcanonical partition function. Note that $N_{\rm ind}$ is the number of independent degrees of freedom [55,56] arising from the gauge-fixing constraint $\mathcal{C}(\pi)=0$ (See Appendix A 2 for further details). Thus, the expectation value of any LGT observable, $\mathcal{O}[\pi,\phi]$, can be computed as the statistical integral of $\mathcal{O}[\pi,\phi]$ with respect to the microcanonical measure, i.e., $\langle\mathcal{O}\rangle_{\mu c} = \int \mathcal{O}[\pi,\phi]d\rho[\phi,\pi]$. In this work, we compute expectation values exploiting the Hamiltonian structure given by Callaway's formalism, that is, we numerically obtain the solution $(\pi^S_{n,\mu},\phi^S_{n,\mu})$ of the Hamilton equations of motion $d\phi_{n,\mu}/d\tau = \pi_{n,\mu}$, $d\pi_{n,\mu}/d\tau = -g_0^2\partial\mathcal{S}_{\rm W}[\phi]/\partial\phi_{\boldsymbol{n},\mu}$; then, ensuring that the system is ergodic (see Appendix B 1), we are allowed to recast the above-mentioned statistical integral into a time average:

$$\langle\mathcal{O}\rangle_{\mu c} \equiv \lim_{T\to\infty}\frac{1}{T}\int_0^T \mathcal{O}[\pi^S_{n,\mu}(\tau),\phi^S_{n,\mu}(\tau)]d\tau. \tag{2}$$

It should be stressed that the equality (2) holds only if the system is ergodic. In Appendix B 1, we performed an ergodicity check for the $U(1)$ LGT. In general, for non-ergodic systems, the exploration of the phase space can be enhanced by employing hybrid algorithms [32,68]. The thermodynamics of compact electrodynamics in the microcanonical ensemble can be investigated by introducing the entropy function which is the fundamental microcanonical thermodynamic potential that generates all the observables, and it is defined by $S_{N_{\rm ind}}(E) \coloneqq \log\int\delta(\mathcal{H}[\pi,\phi]-E)\delta(\mathcal{C}(\pi))D\pi D\phi$ with $k_B=1$. Within this framework, we can investigate the thermodynamic properties of the $U(1)$ LGT adopting the MIPA [13,15,16]. According to MIPA, PTs are split into two classes: independent and dependent. Independent PTs represent the major change in the system's phase, whereas a dependent PT can only occur if an independent one already manifested; therefore, they are considered the precursors of a major transition. An independent PT of even (odd) order $2n$ $(2n-1)$ occurs at E_c if $\partial_E^{2n-1}S_N$ $(\partial_E^{2n-2}S_N)$ admits an inflection point at E_c and $\partial_E^{2n}S_N$ $(\partial_E^{2n-1}S_N)$ combined with a negative-valued maximum (positive-valued minimum) at E_c. A dependent PT of even (odd) order $2n$ $(2n+1)$ is detected at E_c, if $\partial_E^{2n-1}S$ $(\partial_E^{2n}S)$ admits a least-sensitive inflection point at E_c combined with positive-valued minimum (negative-valued maximum) at $\partial_E^{2n}S$ $(\partial_E^{2n+1}S)$ [16]. We present here the application of MIPA for the $U(1)$ LGT with lattice $N=12^4$. In Appendix F, we show a comparison of the thermodynamic observables for different systems' sizes: $N=6^4, 8^4, 10^4$ and 16^4 together with an analysis about the stability of the PT as a function of N. The computation of entropy derivatives, necessary for employing MIPA, has been performed numerically, by adopting the method in Ref. [69] which allows one to estimate any n-order derivative of the microcanonical entropy through the time average defined in Eq. (A4) of polynomials of the kinetic energy. For instance, $\partial_E S(E) = (N_{\rm ind}/2-1)\langle K^{-1}\rangle_{\mu c}$ (see Appendix C 1 a for higher-order derivatives). In the top panel of Fig. 1, we present the first-order derivative of (specific) entropy $\partial_\varepsilon s$ as a function of energy density, $\varepsilon = E/N_{\rm ind}$ (see Appendix C 1 a for deeper details). Note that it coincides with the inverse of microcanonical temperature $\beta_{\mu c}$. We can easily identify a back-bending region (S shape) in $\partial_\varepsilon S(=\beta_{\mu c})$ entailing a positive-valued minimum at $\varepsilon_1^{\rm ind}\approx 1.2019$ identified by the vertical dot-dashed red line. Such a minimum corresponds to a positive-valued maximum in $\partial_\varepsilon^2 S$ (see Fig. 1), thus to an independent first-order PT, according to MIPA. Such a transition corresponds to the DPT. Indeed, the value of $\beta_{\mu c}$ at the transition point $\varepsilon_1^{\rm ind}$ corresponds to $\partial_\varepsilon S(\varepsilon_1^{\rm ind}) \equiv \beta(\varepsilon_1^{\rm ind}) = 1/T_1 \approx 1.0086$ which coincides with the transition value of β predicted by Monte Carlo simulations [55,56,62,65,70,71]. It should be stressed that the DPT has sometimes been classified as a second-order PT [57,70–75], but many observations, such as the emergence of metastable states, are led to conclude that the DPT is of first order [43,44,62–66]. To confirm the identification of such a first-order PT with the DPT, we provide the microcanonical computation of the average plaquette per (independent) degree of freedom, $\langle\bar{\mathcal{V}}_\square\rangle_{\mu c} = g_0^2\langle\mathcal{S}_W(\boldsymbol{\phi})\rangle_{\mu c}/N_{\rm ind}$ as a function of the microcanonical temperature, as suggested in Ref. [55]. As shown in the plot on the right in Fig. 8 in Appendix C, the average plaquette becomes a multivalued function that admits an S shape around $\beta_1\approx 1.0086$ (see the inset); this is a typical signature of a first-order PT. It should be noted that such an S shape is a direct consequence of the inflection point in $\partial_\varepsilon S$. In particular, the local minimum associated with the DPT $(\partial_\varepsilon S|_{\varepsilon_1}=0)$ is the deep origin of the vertical tangent point indicated by the vertical red line on the right panel of Fig. 8 in Appendix C. Following MIPA, we can identify a further third-order independent PT, associated with an inflection point in $\partial_\varepsilon^2 S$ (see the vertical blue line in Fig. 1) together with a positive-valued minimum in $\partial_\varepsilon^3 S$ around $\varepsilon_3^{\rm ind}\approx 1.028$ (see Fig. 2). Furthermore, we have evidence that supports the identification of an additional third-order dependent PT occurring at $\varepsilon_3^{\rm dep}\approx 1.2645$ (see the green line in the panel on the right of Fig. 1). A deeper analysis of such a PT is presented in the Appendix F. Interestingly, we do not find this transition for a small system's size but it appears at

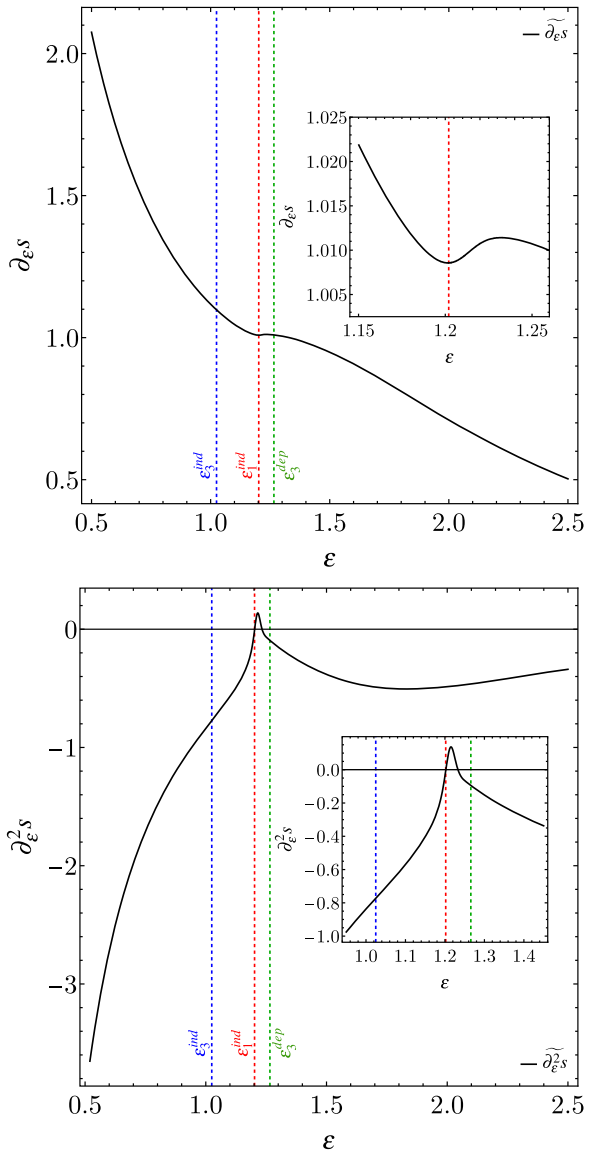

FIG. 1. First- and second-order derivative of entropy for the 4D $U(1)$ LGT with lattice size $N = 12^4$. In the top panel, the first-order derivative of entropy is plotted as a function of the specific energy. In the inset, an enlargement of the same observable around the DPT is reported so as to visualize the positive-valued minimum. In the bottom panel, the first-order derivative of entropy is plotted as a function of the specific energy. In the inset, an enlargement of the same observable around the DPT is reported. All of the PTs discussed in the main text are represented in the plot by vertical lines: an independent third-order PT $\varepsilon_3^{\rm ind}$ (blue dashed line), an independent first-order PT $\varepsilon_1^{\rm ind}$ (red dashed line), and a dependent third-order PT $\varepsilon_3^{\rm dep}$ (green dashed line).

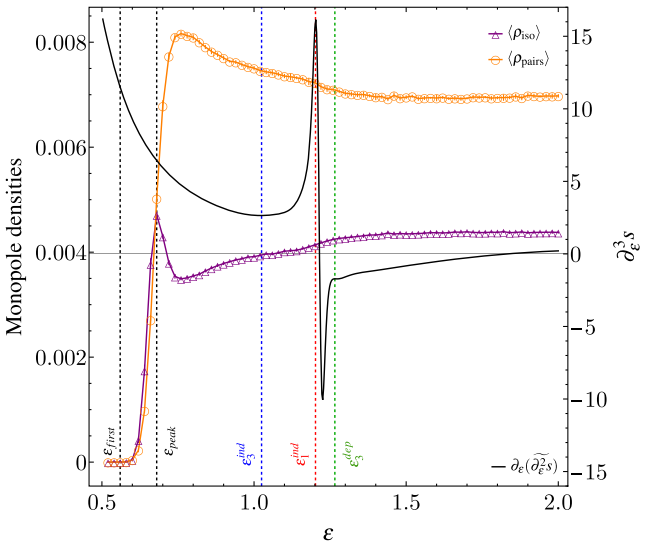

FIG. 2. Comparison between third-order derivative and density of monopoles for the 4D $U(1)$ LGT with lattice size $N = 12^4$. The black curve represents $\partial_\varepsilon^3 S$ obtained by analytical derivation of the rational fitting function of the second-order derivative of entropy. The orange and violet curves represent the number density of monopole-antimonopole pairs and isolated monopoles, respectively. The vertical colored lines indicate the energy value of each PT as defined in Fig. 1.

larger sizes ($N \geq 12$). To understand the physical meaning of these new PTs identified by MIPA and never observed so far, we analyze and compare the third-order derivative of the microcanonical entropy with the average number density of topological defects. The current knowledge of the role of topological defects during the DPT is summarized in Ref. [47]: at $T < T_1$, there are few monopole loops, and they will be small in the spatial extent. Increasing T increases the density and size of the loops. At T_1, the monopole-antimonopole pairs dissolve, and the theory's vacuum becomes a gas of monopoles and antimonopoles without strong correlations. In light of our results, we numerically demonstrate that the spectrum of transitional/collective phenomena occurring in $U(1)$ LGT is richer than the expected one. Indeed, the paradigm associated with the pair dissolution should be revisited. In other words, the DPT is not a "sharp" process where pairs completely disappear crossing the critical temperature/energy threshold. Conversely, this process manifests through a sequence of phenomena, and at high energies (or temperatures) the monopole pairs do not completely disappear. To see that, we analyze the energy behavior of the density of topological defects, i.e., we consider the 3D monopoles of the gauge field as defined in Refs. [41,76] (see Appendix G for more details). In particular, we compute the average densities of monopole-antimonopole pairs at the nearest-neighbor distance, $\langle\rho_{pair}\rangle$, of isolated monopoles, $\langle\rho_{\rm iso}\rangle$, and of the average density of the total number of monopoles and antimonopoles, $\langle\rho_{\rm tot}\rangle$. These behaviors are reported in Fig. 2 by the yellow and violet curves, respectively. The phenomenology behind this process can be summarized as follows. For energies $\varepsilon \leq 0.56$, monopoles are not detected, and $\langle\rho_{\rm iso}\rangle = \langle\rho_{\rm pairs}\rangle = 0$ and their first appearance, i.e., nonvanishing

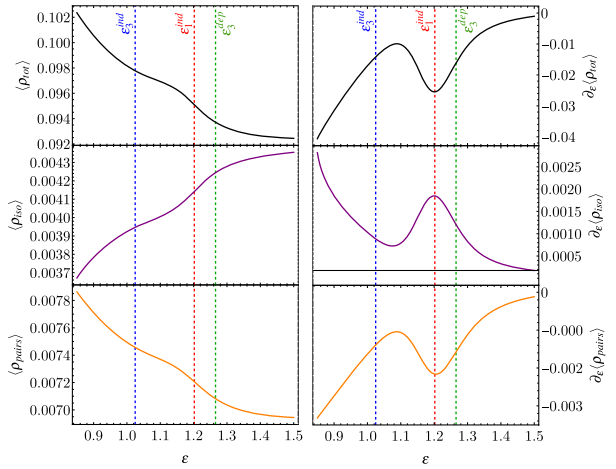

FIG. 3. Monopole densities and their derivatives around the deconfinement transition for LGT U(1) for $N = 12$. In the left panel, the density of monopoles $\langle \rho_{\rm tot} \rangle$ (black line), the density of isolated monopoles $\langle \rho_{\rm iso} \rangle$ (purple line), and the density of monopole pairs $\langle \rho_{\rm pairs} \rangle$ (orange line) as obtained by fitting the numerical data with a rational function are reported. In the right panel, the derivatives of the respective quantities are reported.

values for $\langle \rho_{\rm iso} \rangle$ and $\langle \rho_{\rm pairs} \rangle$, occurs around $\varepsilon_{\rm first} \approx 0.56$ (see the inset in Fig. 2). For energies slightly larger than $\varepsilon_{\rm first}$, only a small number of monopoles is found to form pairs; the largest amount of monopoles is in the isolated configuration, i.e., the free states. Increasing the energy, $\langle \rho_{\rm iso} \rangle$ reaches a local maximum around $\varepsilon_{\rm peak} \approx 0.68$. Thus, in the interval $\varepsilon_{\rm first} \leq \varepsilon \leq \varepsilon_{\rm peak}$, the production of isolated monopoles is favored over that of pairs up to $\varepsilon_{\rm peak}$ where such a production ends. For $\varepsilon_{\rm peak} \leq \varepsilon$, the process reverses: the isolated monopoles begin to interact *leaving* the isolated configuration to form pairs as one deduces from the subsequent drop of $\langle \rho_{\rm iso} \rangle$. At this stage, the production of pairs increases, reaching a peak at $\varepsilon \simeq 0.76$, and this process corresponds to the saturation of the pair-production process; pairs mostly populate the vacuum state of the theory. From that moment on, we observe the pair-dissolution process where the number density of pairs $\langle \rho_{\rm pairs} \rangle$ decreases in energy. During this process, three PTs are involved, and they manifest at energy values where the functions $\langle \rho_{\rm pairs} \rangle$ and $\langle \rho_{\rm iso} \rangle$ change their concavities as shown in Fig. 3. By going over $\varepsilon_3^{\rm ind}$, $\langle \rho_{\rm pairs} \rangle$ passes from having positive to negative concavity so as $\partial_\varepsilon \langle \rho_{\rm pairs} \rangle$ manifests a maximum. Analogously, $\langle \rho_{\rm iso} \rangle$ passes from having negative to positive concavity so as $\partial_\varepsilon \langle \rho_{\rm iso} \rangle$ manifests a minimum. Then, the concavity changes again crossing the threshold $\varepsilon_1^{\rm ind}$ and, above the (alleged) dependent third-order PT, the monopole densities become flat. The physical meaning of the two concavity changes can be associated, respectively, to a slowdown and an acceleration of the pair-dissolution process which, in turn, terminates with a plateau indicating the end of such a process. The slowing-down phase culminates with the third-order independent PT associated with the positive-valued minimum in $\partial_\varepsilon^3 S$ (blue vertical line). After that point, the number density of pairs decreases, accelerating up to the deconfinement PT where $\langle \rho_{\rm pairs} \rangle$ decreases decelerating. We conclude noting that our analysis provides a qualitative agreement between the maxima/minima of the pairs/monopole density derivative that brings out the role of topological defects in transitional phenomena. In the next work, we aim to reach also the quantitative agreement reducing the mismatch observed in Fig. 3 between the energy corresponding to the maximum (minimum) in $\partial_\varepsilon \langle \rho_{\rm pairs} \rangle$ ($\partial_\varepsilon \langle \rho_{\rm iso} \rangle$) and $\varepsilon_3^{\rm ind}$.

In summary, we have shown that the application of MIPA to a microcanonical formulation of the $U(1)$ LGT allowed us to identify, besides the DPT, two further PTs: an independent (major) third-order PT and a dependent (minor) third-order PT. We found a direct connection between the emergence of these transitional phenomena and the energy dynamics of the topological defects. Interestingly, we could interpret the presence of the dependent PT occurring in the Coulomb phase as the evidence of a further phase separation within the Coulomb phase, distinguishing a "weak" and a "strong" Coulomb phase. The latter can be interpreted as a pure deconfined phase occurring in the range $\varepsilon > \varepsilon_3^{\rm dep}$ and signaled by the beginning of the plateau of the pair number density (and of the isolated monopole density as well). What we interpreted as a "weak" deconfined phase, instead, occurs in the range $\varepsilon_1^{\rm ind} < \varepsilon < \varepsilon_3^{\rm dep}$, and it is characterized by an increasing of the production rate of the number of pairs as suggested by Fig. 3. Such a result stimulates future investigations for confirming a new phase separation in the deconfined phase in correspondence of the third-order dependent PT at $\varepsilon_3^{\rm dep}$.

We conclude by stressing that the analysis presented in this paper is not restricted to pure LGTs; we propose to extend the new paradigm for the investigation of PTs provided by the microcanonical analysis to non-Abelian LGTs interacting with fermions. For this purpose, one can adopt the microcanonical algorithms of Kogut [61,77] and Duane [78], so as to compute microcanonical observables (the derivatives of entropy) and thus apply MIPA to search for new PTs. Moreover, the similarity between the Abelian gauge theory and the Heisenberg model [40,79] encourages the application of MIPA to many condensed-matter systems. In this respect, MIPA and the analysis of the topological defects can be used for better understanding the topological origin of glass transition [80,81], transitions in spin liquids [82,83], and the transition observed experimentally [84–86] in exotic magnets called spin ices [87,88] due to the emergence of magnetic monopoles. Finally, MIPA can provide further insights into the recent investigation of the interplay between the Casimir effect, the deconfinement PT, and the emergence of monopoles [89–92].

The authors thank Dr. Matteo Barborini for his contribution to code development, optimization, and for his valuable insights. The calculations presented in this paper were carried out using the HPC facilities of the University of Luxembourg [93] (see [94]) and those of the Luxembourg national supercomputer MeluXina. The authors gratefully acknowledge the LuxProvide teams for their expert support. This research was funded in whole, or in part, by the Luxembourg National Research Fund (FNR), grant reference BroadApp C20/MS/14769845, and by HEurope ERC-AdG 101054629-FITMOL.

APPENDIX A: HAMILTONIAN MODEL FOR THE U(1) COMPACT MODEL ON 4D EUCLIDEAN LATTICE: NUMERICAL ALGORITHM

The investigation of the thermodynamic properties of the $U(1)$ LGT is based on the molecular dynamics simulation of the Hamiltonian system defined by

$$\mathcal{H}(\pi,\phi) \coloneqq \sum_{\mu,n}\frac{\pi_{n,\mu}^2}{2} + \sum_{\square_{\mu,n}}[1-\cos(\phi_{\boldsymbol{n},\mu}+\phi_{n+\mu,\nu}-\phi_{n+\nu,\mu}-\phi_{n,\nu})], \tag{A1}$$

where $\square_{\mu,\nu,n}$ is a representative plaquette. We then numerically solved the Hamilton equations of motion,

$$\frac{d\phi_{\mu,n}}{d\tau}=\pi_{\mu,n}, \qquad \frac{d\pi_{\mu,n}}{d\tau}(\tau)=-\frac{\partial\mathcal{H}}{\partial\phi_{\mu,n}}, \tag{A2}$$

adopting a second-order bilateral symplectic algorithm [95] since it conserves the symplectic structure of the Hamiltonian flow.

1. Integration scheme

The implemented algorithm reads as ($\tau_{n/2}\coloneqq\tau_0+n\Delta\tau/2$):

$$\begin{aligned}
\phi_{\mu,n}(\tau_{1/2}) &= \phi_{\mu,n}(\tau_0),\\
\pi_{\mu,n}(\tau_{1/2}) &= \pi_{\mu,n}(\tau_0) - F_{\mu,n}[\phi(\tau_{1/2})]\Delta\tau/2,\\
\phi_{\mu,n}(\tau_1) &= \phi_{\mu,n}(\tau_{1/2}) + \pi_{\mu,n}(\tau_{1/2})\Delta\tau,\\
\pi_{\mu,n}(\tau_1) &= \pi_{\mu,n}(\tau_{1/2}) - F_{\mu,n}[\phi_1]\Delta\tau/2,\\
\pi_{\mu,n}(\tau_{3/2}) &= \pi_{\mu,n}(\tau_1),\\
\phi_{\mu,n}(\tau_{3/2}) &= \phi_{\mu,n}(\tau_1) + \pi_{\mu,n}(\tau_{3/2})\Delta\tau/2,\\
\pi_{\mu,n}(\tau_2) &= \pi_{\mu,n}(\tau_{3/2}) - F_{\mu,n}[\phi(\tau_{3/2})]\Delta\tau,\\
\phi_{\mu,n}(\tau_2) &= \phi_{\mu,n}(\tau_{3/2}) + \pi_{\mu,n}(\tau_{3/2})\Delta\tau,
\end{aligned} \tag{A3}$$

where $F_{\mu,n}(\tau)\coloneqq\partial_{\phi_{\mu,n}}\mathcal{V}[\phi(\tau)]$. The time step has been chosen to be $\Delta\tau=0.001$ according to the analysis presented in Appendix B 2. With this choice, the energy is conserved with a precision of 10^{-8}–10^{-9}.

2. Initial conditions and energy selection

The initial conditions for the system have been chosen following a specific procedure that we are going to explain. Initially, we associate random values for $\phi_{\mu,n}$, and we set $\pi_{\mu,n}=0$ for every n and μ. The choice of zero values for the momenta has been proposed by Callaway in Refs. [55,56] and must be interpreted as a method aimed at eliminating the extra degrees of freedom coming from the gauge invariance. This procedure is indeed equivalent to imposing a gauge such as, for instance, the Lorentz gauge, the axial one, the Landau gauge, and so on and so forth. Thus, owing to this constraint, the number of independent degrees of freedom used in our calculation is $N_{\rm ind}=3\cdot N^4$ where N is the number of sites of the lattice.

In this way, we obtain an energy value, E_{rand}, that we do not control *a priori* due to the random initialization of $\phi_{\mu,n}$. Before reaching the desired energy, we allowed the system to evolve for 10^4 steps so as to equilibrate the trajectory. Then, starting from E_{rand}, we reach the desired energy, say $E_{\rm des}$, searching for a suitable constant α such that, multiplying each momentum $\pi_{\mu,n}$ by α, the system is heated for $\alpha>1$ or cooled for $\alpha<1$. In practice, we make a guess $\alpha_{\rm guess}$ and measure $E_{\rm guess}=\mathcal{H}[\alpha\pi_{\mu,n},\phi_{\mu,n}]$. This procedure is repeated as long as $|E_{\rm guess}-E_{\rm des}|$ is smaller than the chosen precision (we have set 10^{-12}).

3. Production run and averages

Once the desired energy has been reached, the system is equilibrated again for 10^6 iterations before saving the trajectory used for computing averages. For each energy value, we have produced $N_{\rm trj}=8$ trajectories using the procedure illustrated in *Initial conditions and energy selection* with different random values. This process has been repeated for each specific energy value $\varepsilon=E/N_{\rm ind}$ within the range [0.50, 2] with a sampling $\Delta\varepsilon=0.02$.

Each thermodynamic observable has been evaluated on $N_{\rm samp}=10^6$ measurements sampled every $N_{\rm step}=800$ steps. The definition of the microcanonical average is based on the ergodic assumption that, adapted to simulations, reads as

$$\langle f\rangle_\varepsilon=\frac{1}{N_{\rm samp}\cdot N_{\rm ind}}\sum_{i=1}^{N_{\rm trj}}\sum_{n=1}^{N_{\rm samp}}f_i(\tau_n), \tag{A4}$$

where $f_i(\tau_n)$ is the observable associated to the ith trajectory at the (fictitious) time τ_n. We note that the ergodic property for this system has been checked and discussed in the upcoming section.

APPENDIX B: CONTROL ANALYSIS

1. Ergodicity

In order to check whether the Hamiltonian system defined by (A1) is ergodic, we analyze the thermodynamic observables extrapolated from simulation data, that is, the first- and second-order derivative of entropy (see Appendix C 1), at three different energies: 0.50, 1.20, 2.00, for a lattice with size 3^4. We notice that the choice of the values of the specific energy has been done depending on the location of the deconfinement PT which is found around $\varepsilon_1^{\mathrm{ind}} \approx 1.2$. Thus, we have chosen two other values of the specific energy far from the main PT. Moreover, it should be stressed that the choice of a small lattice size is based on the fact that the ergodicity is a property of the system that is present (or not) independently by the number of degrees of freedom. In particular, if the system is not ergodic for low values of N_{ind}, then, it will not be ergodic for large of N_{ind}. For each value of the specific energy, we produced 100 realizations, that is, $N_{\mathrm{trj}} = 100$ trajectories with different initial conditions. We first evolved the trajectories for a number of 10^6 MD steps before saving the configurations so as to better "forget" the initial conditions. Then, we have computed the microcanonical observables of interest, that is, for $j \in [1, N_{\mathrm{trj}}]$, we denote with $f_1^\varepsilon(j) \coloneqq \partial_\varepsilon S_j$ and $f_2^\varepsilon(i) \coloneqq \partial_\varepsilon^2 S_j$ the sequences of numbers obtained from simulations.

At this stage, given a certain value of the specific energy, we interpret each number of the sequences $\{f_1^\varepsilon(j)\}_j$ and $\{f_2^\varepsilon(j)\}_j$ as an independent realization of an underlying stochastic process, and we construct the associated histogram centered around the mean values of the sequences. For this scope, we use the function HistogramDistribution implemented in the *Mathematica* software. The histograms have been thus used for extrapolating the probability distribution function (PDF) of the process. This step has been accomplished using the function FindDistribution in *Mathematica* which returned a normal distribution with mean $\mu = 0$ (the histogram is centered around the mean) and standard deviation σ for each histogram. The values for the standard deviation and the comparison between the histograms and the associated normal distributions are reported in Figs. 4 and 5.

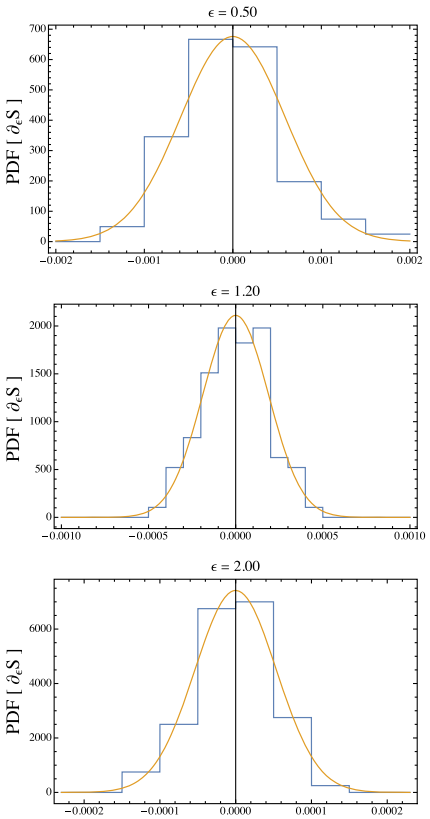

FIG. 4. Histograms associated to the values of the first-order derivative of entropy for three values of the specific energy $\varepsilon = 0.5,\ 1.20,\ 2.00$. The mean value for each histogram and probability distribution function is zero whereas the standard deviation is $\sigma_{\varepsilon=0.5} = 5.90 \times 10^{-4}$, $\sigma_{\varepsilon=1.2} = 1.89 \times 10^{-4}$ and $\sigma_{\varepsilon=2.0} = 5.38 \times 10^{-5}$.

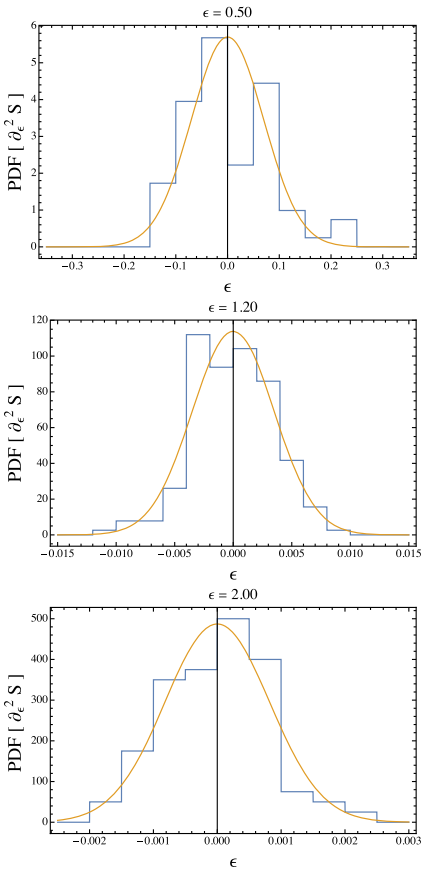

FIG. 5. Histograms associated to the values of the second-order derivative of entropy for three values of the specific energy $\varepsilon = 0.5,\ 1.20,\ 2.00$. The mean value for each histogram and probability distribution function is zero whereas the standard deviation is $\sigma_{\varepsilon=0.5} = 8.47 \times 10^{-2}$, $\sigma_{\varepsilon=1.2} = 3.50 \times 10^{-3}$ and $\sigma_{\varepsilon=2.0} = 8.19 \times 10^{-4}$.

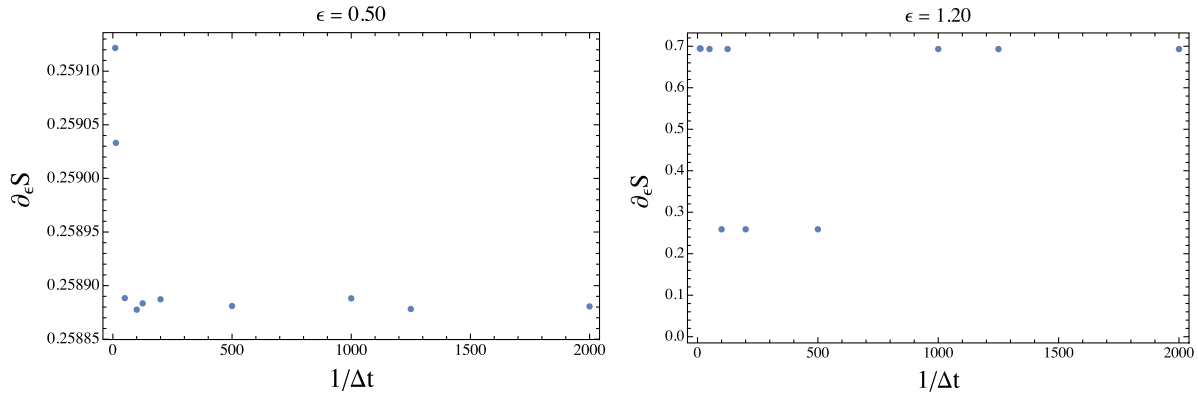

FIG. 6. Plot of first-order derivative of entropy ($\partial_\epsilon s$) vs inverse of the time step ($1/\Delta t$) for specific energy $\varepsilon = 0.50$. A plateau is reached for $\Delta t^{-1} \geq 200$.

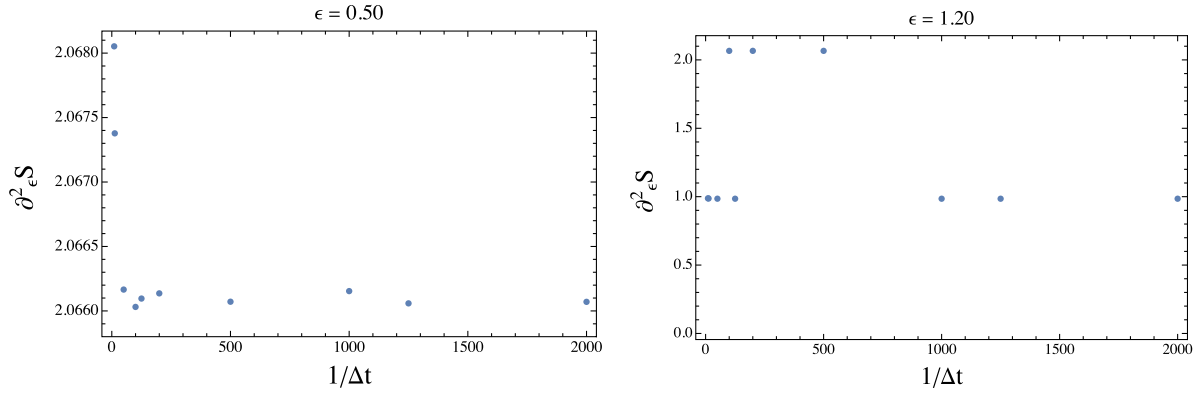

FIG. 7. Plot of second-order derivative of entropy ($\partial_\varepsilon^2 s$) vs inverse of the time step ($1/\Delta t$) for specific energy $\varepsilon = 1.20$. A plateau is reached for $\Delta t^{-1} \geq 1000$.

2. Choice of the time step

In order to find the most appropriate value of the time step, we have produced some trajectories for a lattice of size 3^4 starting from the same initial conditions at two different values of the specific energy: 0.50 and 1.20. More precisely, after the equilibration process performed as explained in Appendix A, we have produced $N_{\mathrm{trj}} = 30$ trajectories for each time step: 0.1, 0.08, 0.02, 0.01, 0.008, 0.005, 0.002, 0.001, 0.0008, 0.0005 adapting the sampling in order to have the same number of points $N_{\mathrm{samp}} = 10^6$ for doing statistics. On these sets of points, we have computed the statistical average for $\partial_\varepsilon S$ and $\partial_\varepsilon^2 S$ according to Eq. (A4). In Figs. 6 and 7, we report the results of this analysis. Focusing on the plots for $\varepsilon = 0.50$, we can see that for $\Delta t \leq 0.005$, the thermodynamic observables reach a certain stability, and their values oscillate with an error of order 10^{-6}. Around the transition energy, i.e., $\varepsilon 1.20$, instead, the stability in the time step is reached for smaller values. In this case, a time step equal to $\Delta t \leq 0.001$ is necessary in order to have a good estimation of the thermodynamic observables.

In light of this analysis, all the simulations have been performed with a time step of $\Delta t = 0.001$.

APPENDIX C: MICROCANONICAL INFLECTION POINT ANALYSIS FOR A FIXED NUMBER OF DEGREES OF FREEDOM

The MIPA requires a calculation of the derivatives of the specific microcanonical entropy defined as

$$S_{N_{\mathrm{ind}}}(E) = \log \int \delta\big(H(\pi,\phi) - E\big)\delta\big(\mathcal{C}(\pi)\big)\mathrm{D}\pi\mathrm{D}\phi, \qquad \text{(C1)}$$

where the condition $\mathcal{C}(\pi) = 0$ is equivalent to a gauge-fixing condition (see the previous section) and $N_{\mathrm{ind}} = 3N^4$ is the number of independent degrees of freedom [55,56]. The specific microcanonical entropy has been introduced so as to extract extensive quantities and compare systems of different sizes, i.e.,

$$s_{N_{\mathrm{ind}}}(\varepsilon) = \frac{1}{N_{\mathrm{ind}}} S_{N_{\mathrm{ind}}}(N_{\mathrm{ind}}\varepsilon).$$

For simplicity, the subscripts are dropped in what follows if not necessary.

1. Estimation of first- and second-order derivative of microcanonical entropy from microcanonical sampling

The MIPA method requires the estimation of the higher-order derivative of the microcanonical entropy from a microcanonical sampling of the phase space, in order to characterize the presence of inflection points with a sufficient level of accuracy. For this purpose, we have adopted two possible methods: the direct calculation of the higher-order derivatives of the microcanonical entropy from higher moments in the distribution of the inverse (specific) kinetic energy, or the analytical derivation of a rational fit of lower-order derivatives of the microcanonical entropy. In the following subsection, we will present the two methods and a comparison of the results.

a. Higher-order derivatives of the microcanonical entropy from momenta of the inverse kinetic energy distribution

As shown in Ref. [69], in the microcanonical ensemble, given any fixed value of the specific energy, the derivatives of specific entropy can be expressed in terms of the moments of the distribution of the inverse specific kinetic energy $k = K(\boldsymbol{\pi})/N_{\rm ind}$. In this framework, the first- and second-order derivatives of specific microcanonical entropy can be written as

$$
\begin{aligned}
(\partial_\varepsilon s)_{\rm PH}(\varepsilon) &= \left(\frac{1}{2} - \frac{1}{N_{\rm ind}}\right)\langle k^{-1}\rangle_\varepsilon, \\
(\partial^2_\varepsilon s)_{\rm PH}(\varepsilon) &= N_{\rm ind}\left[\left(\frac{1}{2} - \frac{1}{N_{\rm ind}}\right)\left(\frac{1}{2} - \frac{2}{N_{\rm ind}}\right)\langle k^{-2}\rangle_\varepsilon - \left(\frac{1}{2} - \frac{1}{N_{\rm ind}}\right)^2\langle k^{-1}\rangle^2_\varepsilon\right], \\
(\partial^3_\varepsilon s)_{\rm PH}(\varepsilon) &= N^2_{\rm ind}\left[\left(\frac{1}{2} - \frac{1}{N_{\rm ind}}\right)\left(\frac{1}{2} - \frac{2}{N_{\rm ind}}\right)\left(\frac{1}{2} - \frac{3}{N_{\rm ind}}\right)\langle k^{-3}\rangle_\varepsilon - 3\left(\frac{1}{2} - \frac{1}{N_{\rm ind}}\right)^2\left(\frac{1}{2} - \frac{2}{N_{\rm ind}}\right)\langle k^{-2}\rangle_\varepsilon\langle k^{-1}\rangle_\varepsilon \right. \\
&\quad \left. + 2\left(\frac{1}{2} - \frac{1}{N_{\rm ind}}\right)^3\langle k^{-1}\rangle^3_\varepsilon\right],
\end{aligned}
\tag{C2}
$$

where the microcanonical averages have been estimated by Eq. (A4) for each realization of a trajectory. It is worth noting that the standard thermodynamic observables as the microcanonical temperature, $T(\varepsilon)$, and the microcanonical specific heat, $C_v(\varepsilon)$, given by

$$
\begin{aligned}
T_{\mu c}(\varepsilon) &= \beta^{-1}_{\mu c} = (\partial s/\partial\varepsilon)^{-1}, \\
C_{\mu c}(\varepsilon) &= (\partial T(\varepsilon)/\partial\varepsilon)^{-1} \equiv -(\partial s/\partial\varepsilon)^2(\partial^2 s/\partial\varepsilon^2)^{-1},
\end{aligned}
\tag{C3}
$$

are connected to the derivatives of microcanonical entropy and, therefore, they can be computed using Eqs. (C2). In Fig. 8 the microcanonical temperature $T_{\mu c}$ and the microcanonical specific heat $C_{\mu c}$ have been reported for the U(1) LGT for different lattice sizes. Consistently with the MIPA, the deconfinement transition is signaled by a maximum in the microcanonical temperature. It is worth noticing that this translates into a singularlike behavior of the microcanonical specific heat $C_{\mu c}$ at DPT even at *finite sizes*. This is a straightforward consequence of the inequivalence of microcanonical and canonical ensembles for a system exhibiting around first-order PTs (see Appendix H for a more detailed discussion).

b. Interpolation of lower-order derivatives of the microcanonical entropy

Although the method presented above allows one to compute in principle the derivatives of the microcanonical entropy at any order, an accurate estimation of the higher-order derivatives ($k > 3$) required by MIPA is practically very hard to achieve due to the very slow convergence of higher moment distribution of the inverse kinetic energy. However, some information on the higher-order derivatives of the microcanonical entropy can be extracted from the analytic (or numerical) derivation of the lower-order derivatives. To find the best fit for the first derivative of the microcanonical entropy, we optimize for the parameters appearing in the following class of functions:

$$
\widetilde{\partial_\varepsilon s} = f(\varepsilon; n, \boldsymbol{a}, \boldsymbol{b}) = \frac{\sum_{i=0}^{n} a_i x^i}{1 + \sum_{j=1}^{n} b_j x^j}. \tag{C4}
$$

Consistently, the second-order derivative of the microcanonical entropy has been fitted using a function of the form

$$
\widetilde{\partial^2_\varepsilon s}(\varepsilon; n, \boldsymbol{a}, \boldsymbol{b}) = \partial_\varepsilon f(\varepsilon; n, \boldsymbol{a}, \boldsymbol{b}). \tag{C5}
$$

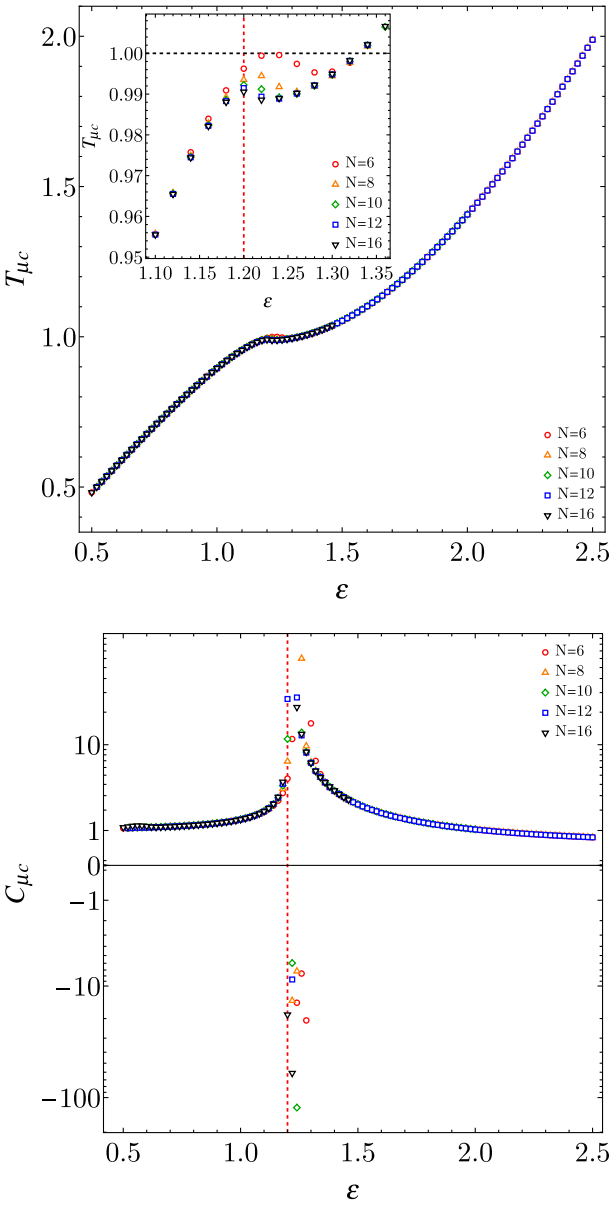

FIG. 8. Thermodynamic observables for U(1) LGT model. In the top panel, the microcanonical temperature $T_{\mu c}$ is reported as a function of the specific energy ε for different lattice sizes. In the bottom panel, the microcanonical specific heat $C_{\mu c}$ as a function of the specific energy ε for different lattice sizes. Distinct symbols represent different datasets: $N = 6$ (red circles), $N = 8$ (orange triangles), $N = 10$ (green diamonds), $N = 12$ (blue squares), and $N = 16$ (black reversed triangles).

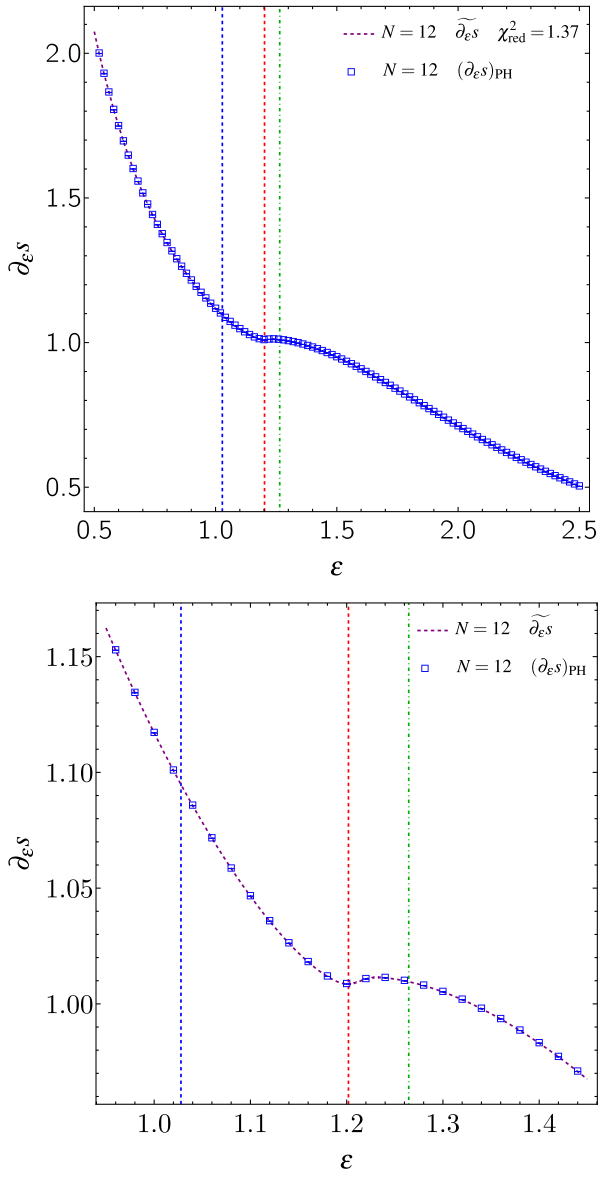

FIG. 9. Analysis of the first-order derivative of the microcanonical entropy for U(1) LGT for lattice size $N = 12$. In top panel, the first-order derivative of the microcanonical entropy as a function of the specific energy as obtained from the Pearson-Halicioglu method $(\partial_\varepsilon s)_{\text{PH}}$ (blue squares) and as obtained from rational interpolation (dashed purple line) is reported. The vertical line is in correspondence with the specific energies of the deconfinement transition (red dashed line), the third-order independent transition (blue dashed), and the third-order dependent transition (green dot-dashed line) as obtained from the best fit of the second-order derivative of microcanonical entropy. In the bottom panel, a zoom of the first-order derivative of the microcanonical entropy as a function of the specific energy is reported on a narrow interval of energies.

APPENDIX D: MIPA FOR $N = 12$

In the following section, we present a detailed analysis exploiting MIPA for compact electrodynamics with $N = 12$. To fit the first-order derivative of entropy, we used a fitting function as in Eq. (C4) with the choice of the hyperparameter $n = 11$. The second-order derivative of the entropy has been fitted using the ansatz in Eq. (C5) with the same choice of parameters M_2 and $\boldsymbol{n}_2$ to perform a direct comparison between the two fits.

From the analysis of the reduced chi-squared, χ^2_{red}, it becomes evident that the rational fit, derived from both the

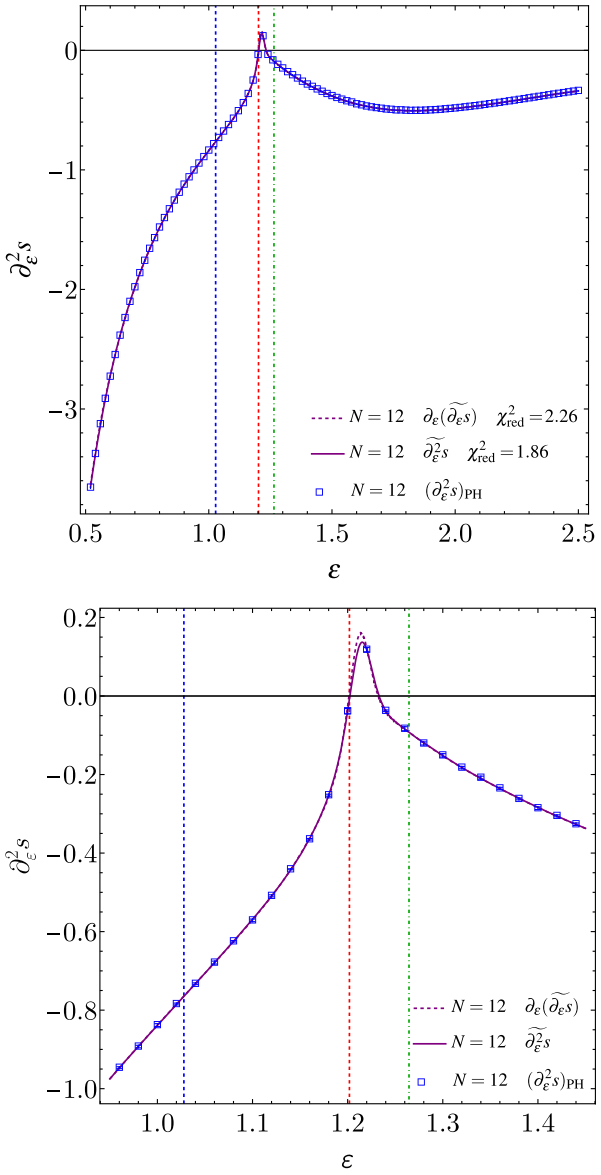

FIG. 10. Analysis of the second-order derivative of the microcanonical entropy for U(1) LGT for lattice size $N = 12$. In the top panel, the second-order microcanonical entropy as a function of the specific energy as obtained from the Pearson-Halicioglu method $(\partial_\varepsilon^2 S)_{\rm PH}$ (blue squares) and as obtained from the analytical derivative of the rational interpolation of first-order microcanonical derivative (dashed purple line), and as obtained from rational interpolation of the $(\partial_\varepsilon^2 S)_{\rm PH}$ (continuous purple line) is reported. The vertical lines are in correspondence with the specific energies of the deconfinement transition (red dashed line), the third-order independent transition (blue dashed), and the third-order dependent transition (green dot-dashed line). In the bottom panel, a zoom of the second-order derivative of the microcanonical entropy as a function of the specific energy is reported on a narrow interval of energies.

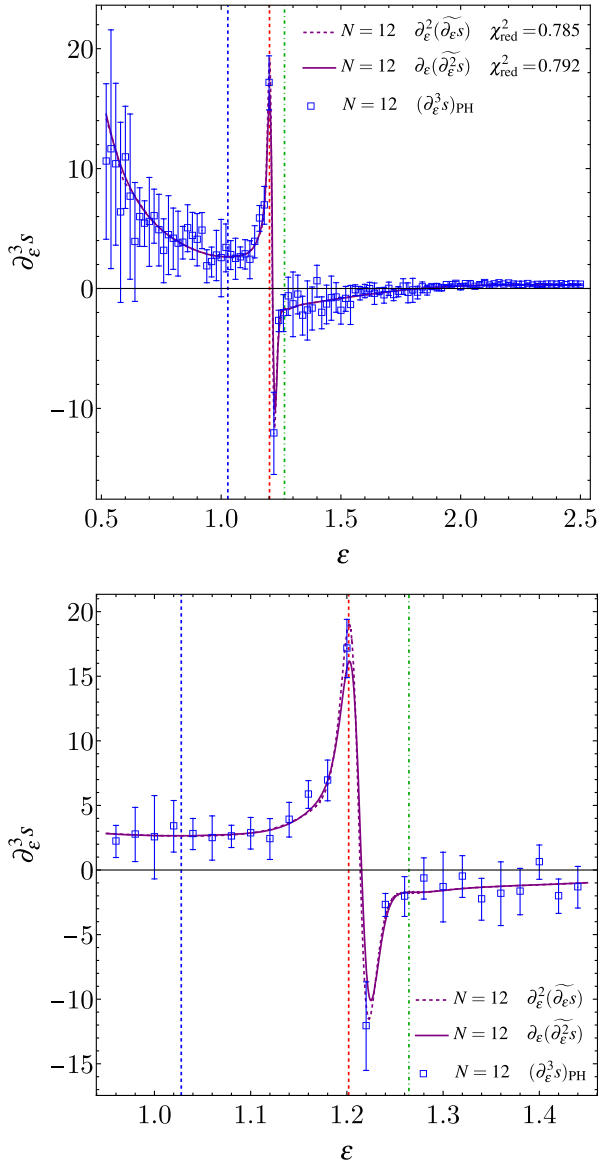

FIG. 11. Analysis of the third-order derivative of the micrcocanoical entropy for U(1) LGT for lattice size $N = 12$. In the top panel, the third-order microcanonical entropy as a function of the specific energy as obtained from the Pearson-Halicioglu method $(\partial_\varepsilon^3 S)_{\rm PH}$ (blue squares) and as obtained from the second-order analytical derivative of the rational interpolation of first-order microcanonical derivative $\partial_\varepsilon^2(\widetilde{\partial_\varepsilon S})$ (dashed purple line), and as obtained from first-order derivative of the rational function interpolating function of the second-order derivative of microcanonical entropy $\partial_\varepsilon(\widetilde{\partial_\varepsilon^2 S})$ (continuous purple line) is reported. The vertical lines are in correspondence of the specific energies of the deconfinement transition (red dashed line), the third-order independent transition (blue dashed), and the third-order dependent transition (green dot-dashed line). In the bottom panel, a zoom of the third-order derivative of the microcanonical entropy as a function of the specific energy is reported on a narrow interval of energies.

first- and second-order derivatives of the entropy, shows an underfitting trend ($\chi^2_{\rm red} \gg 1$). This is due to the small error bars obtained from numerical simulations. The derivatives of the rational functions $\widetilde{\partial_\varepsilon s}$ and $\widetilde{\partial^2_\varepsilon s}$ fit the data obtained numerically of the third-order derivative of the entropy $(\partial^3_\varepsilon S)_{\rm PH}$ with a level of accuracy in agreement with the experimental uncertainties ($\chi^2_{\rm red} \sim 1$). This establishes the self-consistency between the fits of the lower-order of the microcanonical entropy and the numerical results obtained for higher-order derivatives.

The first-order derivative of entropy has a local positive-valued minimum in correspondence with the DPT. According to the MIPA scheme, this corresponds to a first-order independent PT (see Fig. 9). This is confirmed by the presence of a zero in the second-order derivative of entropy (see Fig. 10). From the two interpolating functions $\widetilde{\partial_\varepsilon s}$ and $\widetilde{\partial^2_\varepsilon s}$, we observe a critical value for the deconfinement phase transition at $\varepsilon_1^{\rm ind} = 1.2019 \pm 0.0006$. Analogously, a third-order independent PT is associated with the positive-valued minimum of the third-order derivative of entropy (see Fig. 11) in the energy range $\varepsilon < \varepsilon_1^{\rm ind}$. We estimated the critical energy for this PT at $\varepsilon_3^{\rm ind} = 1.028 \pm 0.007$ by looking at the zeros of the fourth-order derivative of entropy obtained from the rational fitting.

A third-order dependent PT occurring at $\varepsilon_3^{\rm dep} = 1.2645 \pm 0.0011$, is detected through the presence of a negative-valued maximum of the third-order derivative of entropy obtained deriving $\widetilde{\partial^2_\varepsilon s}$ and $\widetilde{\partial_\varepsilon s}$. However, only weak evidence of such a transition can be inferred from our data, as the large errors in the value of $\partial^3_\varepsilon s$ as directly estimated from the microcanonical sampling do not allow one to confirm the presence of a negative maximum.

APPENDIX E: ON THE ORIGIN OF THE S SHAPE IN THE PLAQUETTE POTENTIAL VS MICROCANONICAL ENTROPY

In this section, we investigate the behavior of the plaquette potential $\langle \mathcal{V}_\square \rangle_{\mu c}$ and its numerical derivative with respect to energy $\partial_\varepsilon \langle \mathcal{V}_\square \rangle_{\mu c}$ regarded as functions of specific energy (see Fig. 12 below). Observing such behaviors, we can conclude that in a neighborhood of the deconfinement phase transition, the energy derivative of the average plaquette potential is bounded. This can be better appreciated computing the beta derivative of the average plaquette potential, i.e.,

$$\lim_{\beta_{\mu c}\to\beta_1^+} \frac{\partial \langle \bar{\mathcal{V}}_\square \rangle_{\mu c}}{\partial \beta_{\mu c}} = \lim_{\beta_{\mu c}\to\beta_1^+} \frac{\partial \langle \bar{\mathcal{V}}_\square \rangle_{\mu c}}{\partial \varepsilon} \frac{\partial \varepsilon}{\partial \beta_{\mu c}} = \lim_{\beta_{\mu c}\to\beta_1^+} \frac{\partial \langle \bar{V}_\square \rangle_{\mu c}}{\partial \varepsilon} \left(\frac{\partial S}{\partial \varepsilon}\right)^{-1} \to -\infty. \tag{E1}$$

Now, $\partial_\varepsilon \langle \bar{\mathcal{V}}_\square \rangle$ is positive and bounded on the considered range of energies (see again Fig. 12 below) whereas $\lim_{\beta_{\mu c}\to\beta_1^+} \partial_{\beta_{\mu c}} \varepsilon = -\infty$.

APPENDIX F: COMPARISON OF THE THERMODYNAMIC OBSERVABLES FOR DIFFERENT SYSTEM SIZE

The MIPA analysis has been repeated on different lattice sizes to provide insight into how the deconfinement phase

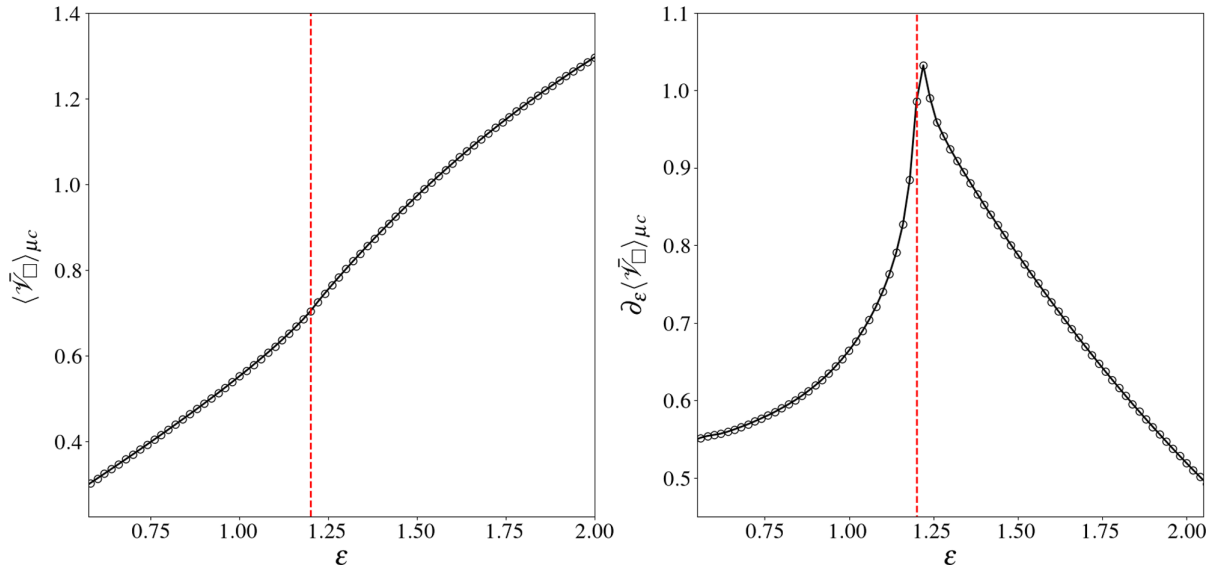

FIG. 12. Microcanonical plaquette potential vs specific energy and its derivative. On the left panel, the microcanonical average of the plaquette potential (black line) and its derivative (blue line) are plotted as functions of the specific energy. The dashed-dotted red line indicates the critical energy, $\varepsilon_1^{\rm ind}$, for the deconfinement transitions. On the right panel, the first-order derivative of the plaquette potential with respect to the specific energy is reported.

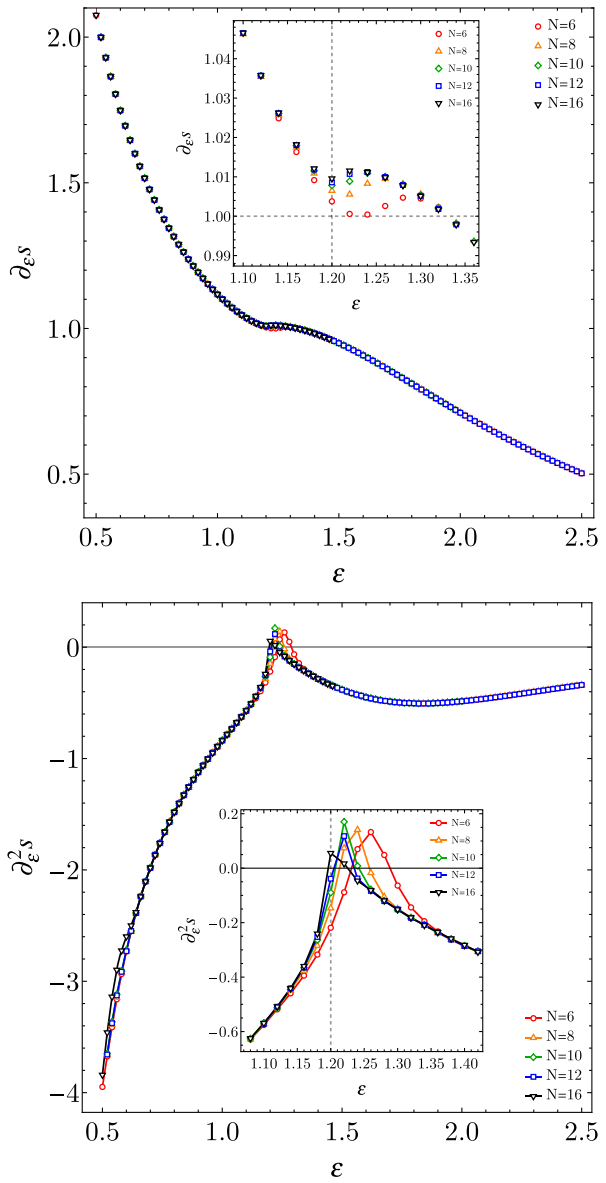

FIG. 13. Comparison of the first- and second-order derivatives of microcanonical entropy as derived from Perason-Halicioglu method. On the top panel, the first-order derivative of the microcanonical with respect to the specific energy of the system for different lattice sizes is reported: $N = 6$ (red circle), $N = 8$ (orange triangle), $N = 10$ (green diamonds), $N = 12$ (blue square), $N = 16$ (black reversed triangle). The region around the deconfinement transition $\varepsilon_1^{\text{ind}} \sim 1.20$ is reported in the inset. A positive minimum of the first-order derivative of the microcanonical entropy corresponding to a first-order order transition is observed for all the lattice sizes. In the bottom panel, the second-order derivative of the microcanonical entropy is reported for the same lattice sizes. In the inset, an enlargement of the region around the deconfinement transition is plotted. A zero of the second-order derivative of the microcanonical entropy can be observed in correspondence with the deconfinement transition for all the investigated lattice sizes.

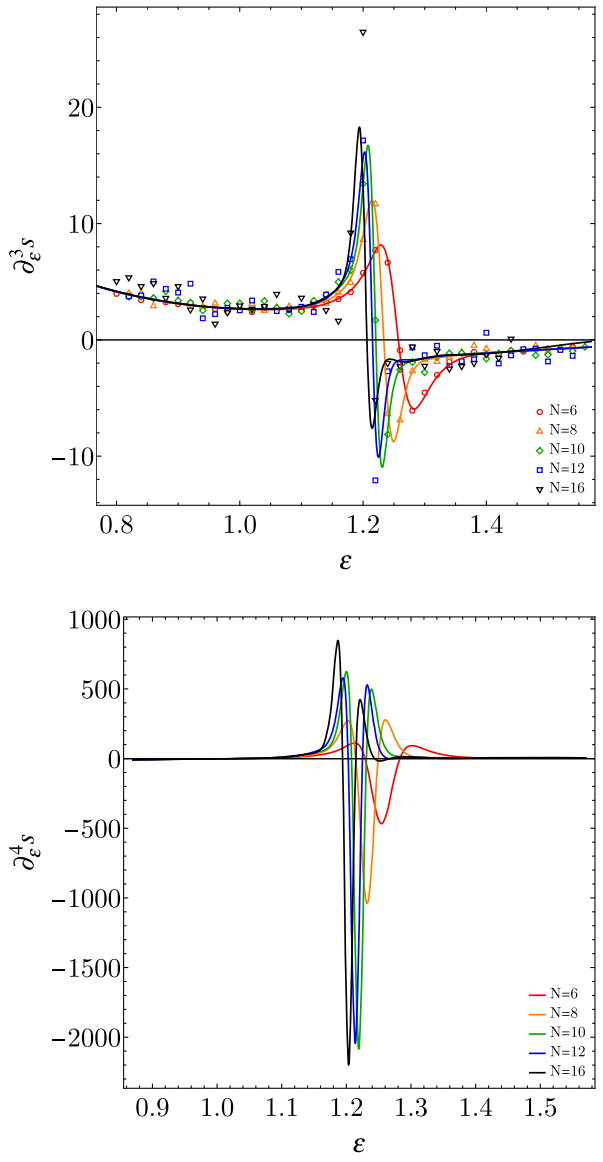

FIG. 14. Third- and fourth-order derivatives of microcanonical entropy for 4D U(1) LGT. In the top panel, the third-order microcanonical entropy, as estimated from the Pearson-Halicioglu method (open markers) and the differentiation of the fitting of the second-order derivative of second-order specific microcanonical entropy (continous line). In the bottom panel, the fourth-order derivative of the microcanonical specific entropy is plotted as a function of specific energy. The different colors refer to different lattice sizes: $N = 6$ (red), $N = 8$ (orange), $N = 10$ (green), $N = 12$ (blue), $N = 16$ (black).

transition and the other higher-order phase transitions identified in the microcanonical ensemble evolve for increasing lattice sizes. Although a detailed analysis of the convergence of the microcanonical entropy is beyond the scope of our current work, we extend the MIPA for different lattice sizes.

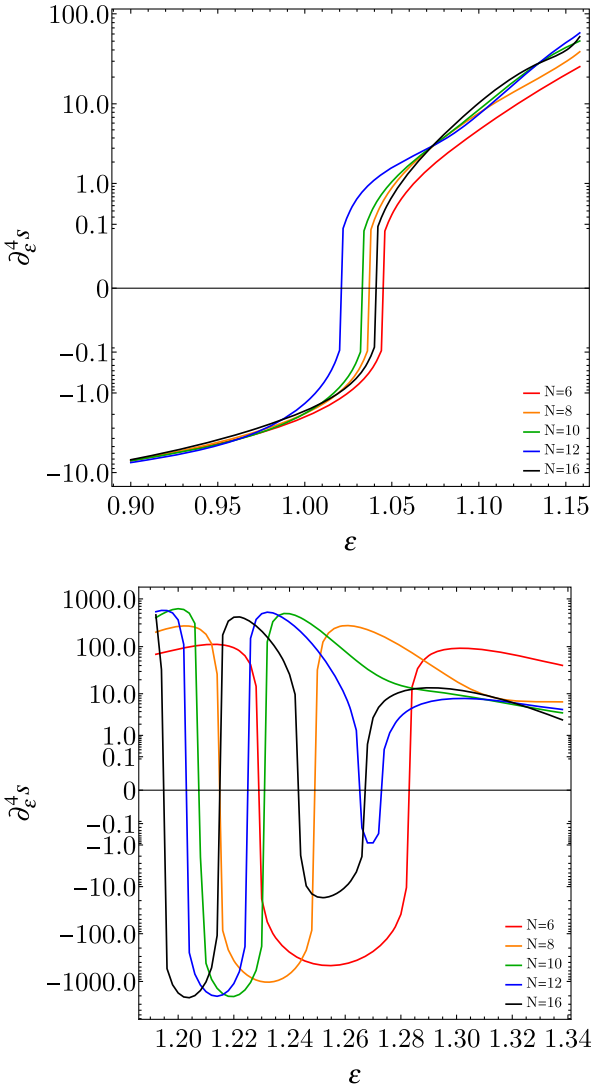

FIG. 15. Characterization of the third-order phase transition in microcanonical U(1) 4D LGT for different lattice sizes. In the top panel, the zero of the fourth-order derivative of the microcanonical entropy corresponding to the third-order independent microcanonical phase transition for different lattice sizes is reported. In the bottom panel, the behavior of the fourth-order derivative of the microcanonical entropy is reported in detail for the region $\varepsilon > \varepsilon_1^{\rm ind}$. The appearance of the third zero around $\varepsilon \approx 1.25$ coincides with the presence of a dependent third-order PT. Note that this transition occurs for larger system's size, i.e., $N \geq 12$. The different colors refer to different lattice sizes: $N = 6$ (red), $N = 8$ (orange), $N = 10$ (green), $N = 12$ (blue), $N = 16$ (black).

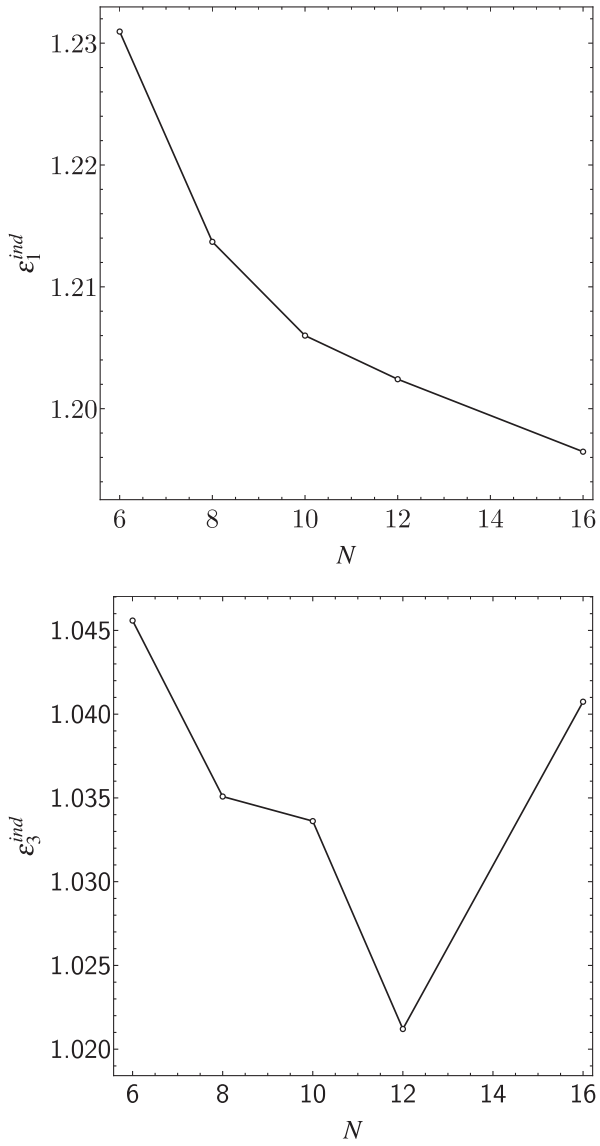

FIG. 16. Critical energies for the first- and third-order independent phase transitions in U(1) 4D LGT for different lattice sizes. In the top panel, the critical energy $\varepsilon_1^{\rm ind}$ of the deconfinement transition is plotted as a function of the lattice size. In the bottom panel, the critical energy $\varepsilon_3^{\rm ind}$ of the third-order independent phase transition in the confined phase is plotted as a function of the lattice size.

In Fig. 13, we present the comparison of the first- and second-order derivatives of the microcanonical entropy for different lattices sizes. For lattice sizes in the range of $6 \leq N \leq 16$, we note the existence of a minimum in the first-order microcanonical entropy around the deconfinement phase transition occurring at $\varepsilon \sim 1.20$. This observation aligns with the behavior of the second-order derivative of the microcanonical entropy, which exhibits a sign change at this point. This change signifies a shift in the concavity of the microcanonical entropy, indicating a first-order (independent) microcanonical phase transition. The scaling of the critical energy $\varepsilon_1^{\rm ind}$, defined as the zero of the analytical estimation of the second-order derivative of the microcanonical entropy, as a function of the lattice size is reported in the top panel of Fig. 16. Moreover, the results seems to indicate a decreasing value of the positive maximum of the second-order derivative of the microcanonical entropy for increasing lattice sizes. This suggests that for larger lattice

sizes there could be a change from a first- to a second-order phase transition for very large lattice sizes.

In Fig. 14 the third- and fourth-order derivatives of the microcanonical entropy are reported for different lattice sizes, in order to investigate higher-order phase transitions.

The estimation of the third-order derivative of the microcanonical entropy from the microcanonical averages of the inverse specific kinetic energy is too noisy for inferring with precision the existence of higher-order phase transitions. For this reason, as in the MIPA analysis for $N = 12$, the third-order derivative of the microcanonical entropy has been estimated from the analytical derivative of the rational function fitting the second-order derivative of the microcanonical entropy. The fourth-order derivative of the microcanonical entropy has been estimated by second-order differentiation of the rational function fitting the second-order derivative of the microcanonical entropy. The analysis of the third-order derivatives of the microcanonical entropy reveals two main features:

(1) A positive minimum of the third-order derivative of microcanonical entropy around $\varepsilon \sim 1.04$ for all the investigated lattice sizes. According to MIPA, this would correspond to the signature of a third-order independent microcanonical phase transition;
(2) The appearance of a negative maximum of the third-order derivative of the microcanonical entropy $\varepsilon \sim 1.26$ for lattice sizes $N \geq 12$, corresponding to a third-order dependent phase transition according to MIPA classification.

These characteristics are confirmed through an examination of the zeros of the fourth-order derivative of the microcanonical entropy, as illustrated in Fig. 15. The convergence of the critical energy pertaining to the third-order independent phase transition has been observed within the considered range of lattice sizes.

The signature of the third-order dependent phase transition is evident only in the analytical derivatives of the rational interpolating function of the second-order derivative of the microcanonical entropy, while the dataset obtained from the microcanonical sampling for the third-order derivative microcanonical entropy is not conclusive in this sense. It is remarkable that in this case, the transition seems to appear only for large lattice sizes.

APPENDIX G: COMPUTATION OF MONOPOLES

The computation of the topological defects used in our work is based on Ref. [41] and reported in Fig. 17. In particular, we studied 3D monopoles redefining the 3D plaquette angle as $\bar{\Theta}_{ij} = \Theta_{ij} - 2\pi K_{ij}$ where $K_{ij} \coloneqq \mod(\Theta_{ij}, 2\pi)$. Then, using Gauss's law, we get

$$N(\boldsymbol{n}) = \sum_{i,j,k=1}^{3} \varepsilon_{ijk}\big(K_{jk}(\boldsymbol{n}+\boldsymbol{e}_i) - K_{jk}(\boldsymbol{n})\big). \quad \text{(G1)}$$

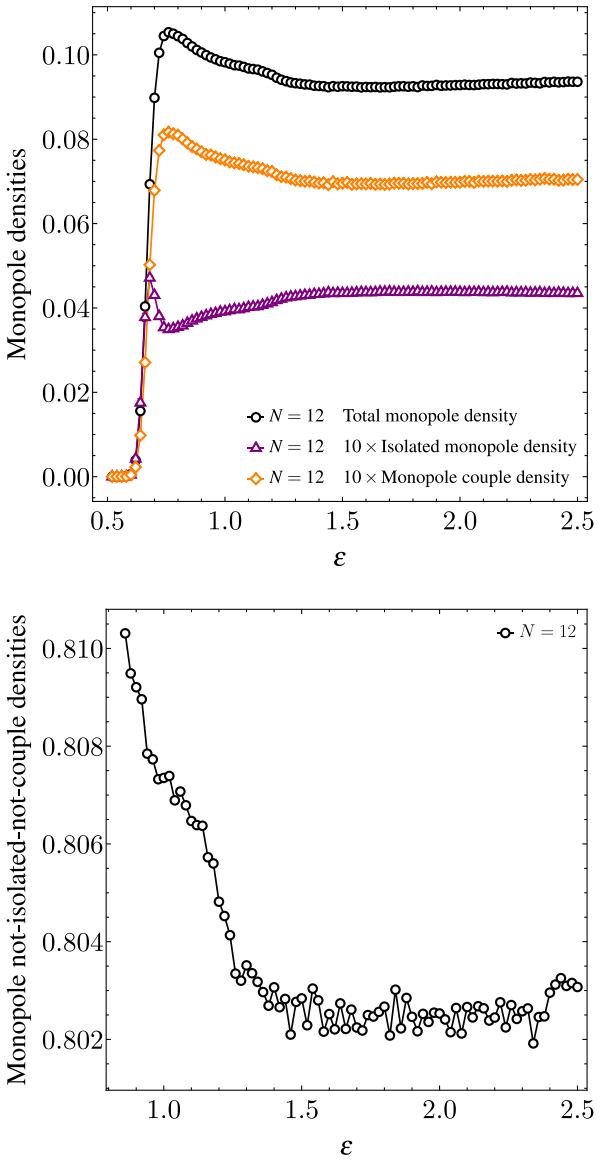

FIG. 17. Analysis of monopole densities for lattice size $N = 12$. In the left panel, the comparison between the monopole density (black circle), the density of isolated monopoles (purple triangle), the density of couples of monopoles (orange diamonds) for different energy values is reported. In the right panel, the density of monopoles that are not isolated nor in a couple as a function of energy is reported.

Here, ε_{ijk} is the Levi-Civita antisymmetric tensor. By definition, $\phi_{\boldsymbol{n},\mu} \in [-\pi, \pi]$ and $\Theta_{ij} \in [-4\pi, 4\pi]$; then, $N = 0, \pm 1, \pm 2$. If $N = 0$ no topological defects are present in the plaquette defined by the site $\boldsymbol{n}$ and the three directions $\boldsymbol{e}_x, \boldsymbol{e}_y$ and $\boldsymbol{e}_z$ whereas if $(N < 0)\, N > 0$ we are in the presence of (anti)monopoles with charge 1 or 2. We study the average density of isolated monopoles $\langle \rho_{\text{iso}} \rangle$ the average density of monopole-antimonopole pairs, and the average density of the total number of monopole and antimonopoles, $\langle \rho_{\text{tot}} \rangle$. The calculation of the former is summarized in the following procedure. At any lattice site, $\boldsymbol{n}$, we identify $N_{\text{iso}}(\boldsymbol{n}) = 1$ if

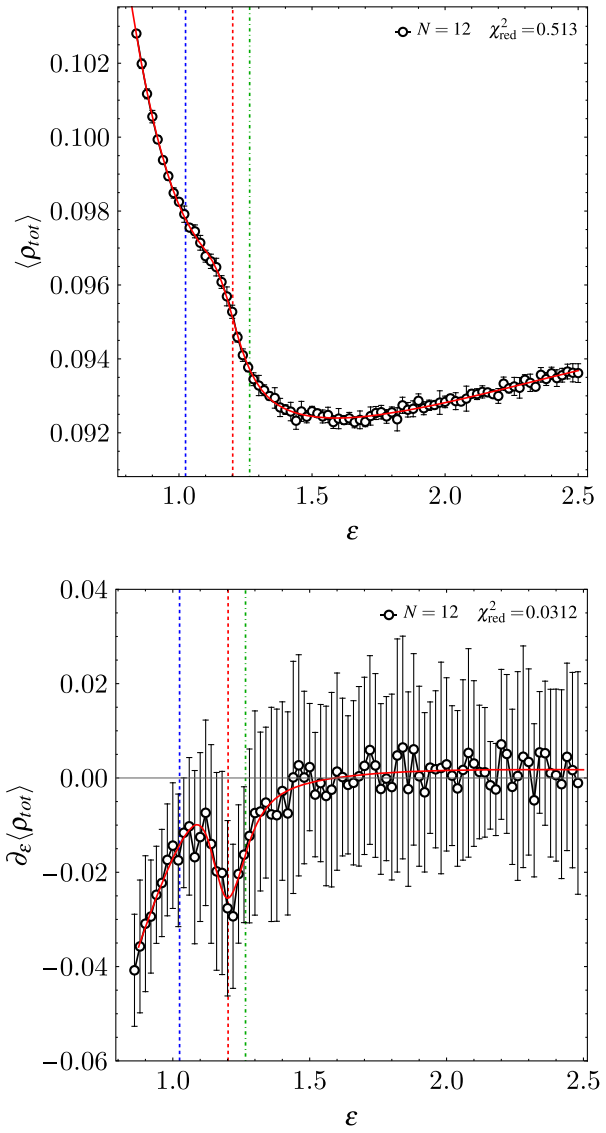

FIG. 18. Analysis of total density of monopoles for lattice size $N = 12$ and for its derivative as a function of the energy. In the left panel, the detail of the total density of monopoles (black circles) around the deconfinement phase transition is reported. The red line is the rational fitting function of the data series. In the right panel, the numerical derivative of the total density of monopoles obtained from finite differentiation (black circle), and the analytic derivative of the interpolating function of the total density of monopoles (red line) are reported. Dashed vertical lines correspond to the phase transition found from MIPA.

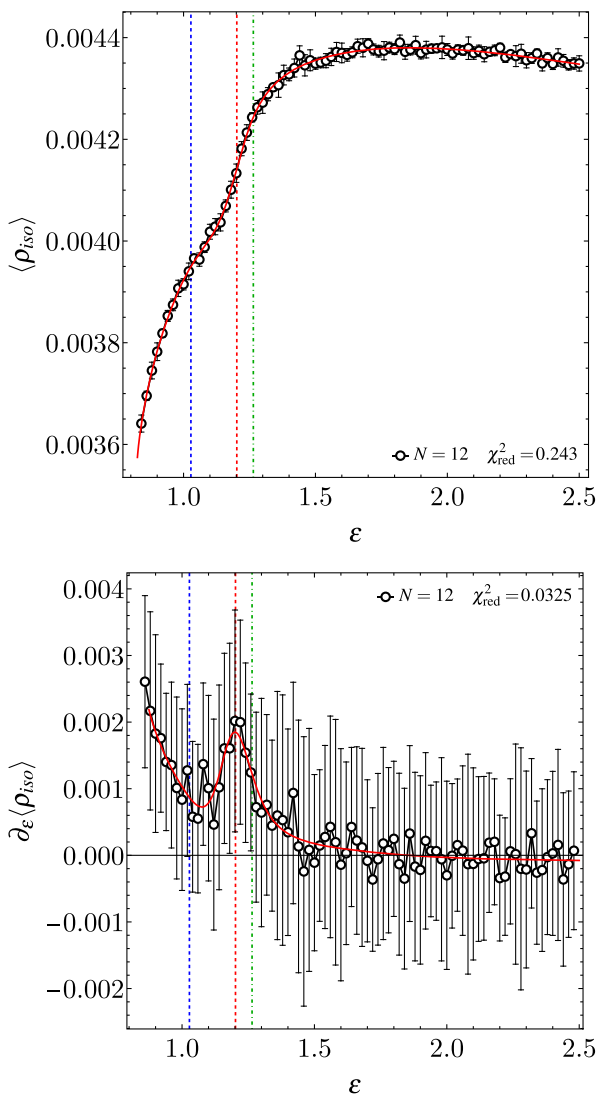

FIG. 19. Analysis of isolated monopole density for lattice size $N = 12$ and for its derivative as a function of the energy. In the left panel, the detail of the density of isolated monopoles (black circles) around the deconfinement phase transition is reported. The red line is the rational fitting function of the data series. In the right panel, the numerical derivative of the density of isolated monopoles as obtained from finite differentiation (black circle) and from the analytic derivative of the interpolating function of the density of isolated monopoles (red line) is reported. Dashed vertical lines correspond to phase transition found from MIPA.

$N(\boldsymbol{n}) \neq 0$, (ii) $N(\boldsymbol{n} \pm \boldsymbol{e}_x) = N(\boldsymbol{n} \pm \boldsymbol{e}_y) = N(\boldsymbol{n} \pm \boldsymbol{e}_y) = 0$. Proceeding in this manner for each lattice site, we define

$$\langle \rho_{\rm iso} \rangle = \frac{1}{V} \sum_{\boldsymbol{n}} N_{\rm iso}(\boldsymbol{n}), \tag{G2}$$

where $V = N^4$ is the volume of the lattice. In our case, $N = 12$. For what concerns the number density of pairs, we proceed similarly as before, but we identify $N_{\rm pair}(\boldsymbol{n}) = 1$ if (i) $N(\boldsymbol{n}) \neq 0$, (ii) $N(\boldsymbol{n} + \boldsymbol{e}_i) = -N(\boldsymbol{n})$ only for a single $i = x, y, z$. Thus, the associated observable is

$$\langle \rho_{\rm pairs} \rangle = \frac{1}{V} \sum_{\boldsymbol{n}} N_{\rm pairs}(\boldsymbol{n}). \tag{G3}$$

Finally, the average density of the total number of monopoles and antimonopoles is defined by introducing $N_{\rm tot}(\boldsymbol{n}) = 1$ if $N(\boldsymbol{n}) \neq 0$ and it is defined by

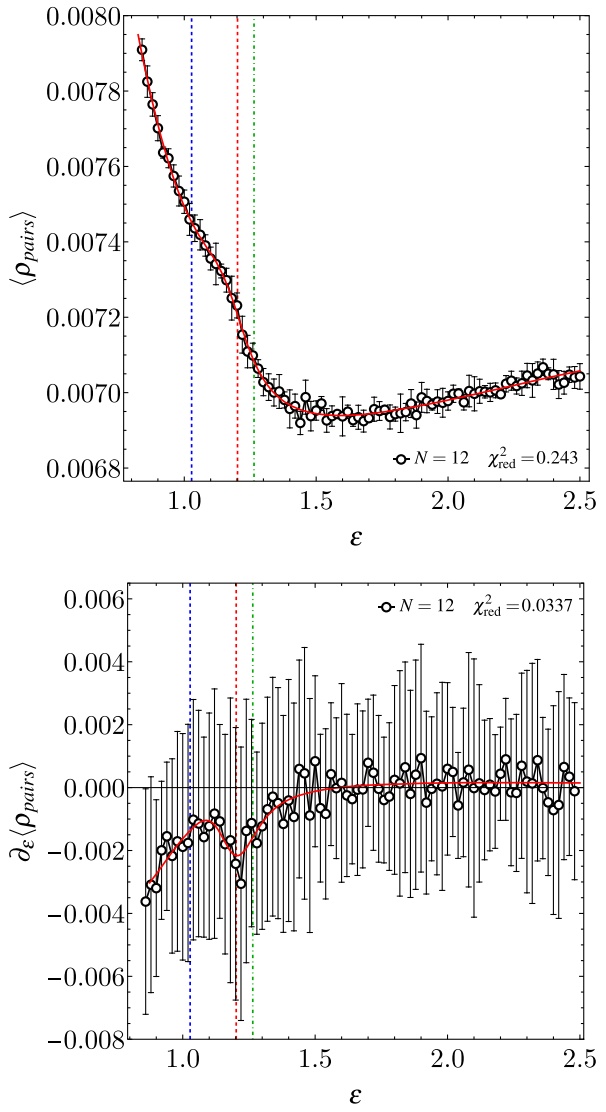

FIG. 20. Analysis of density of couples of monopoles for lattice size $N = 12$ and for its derivative as a function of the energy. In the left panel, the detail of the density of couples of monopoles (black circles) around the deconfinement phase transition is reported. The red line is the rational fitting function of the data series. In the right panel, the numerical derivative of the density of couples of monopoles obtained from finite differentiation (black circle) and the analytic derivative of the interpolating function of the density of couples of monopoles (red line) are reported. Dashed vertical lines correspond to the phase transition found from MIPA.

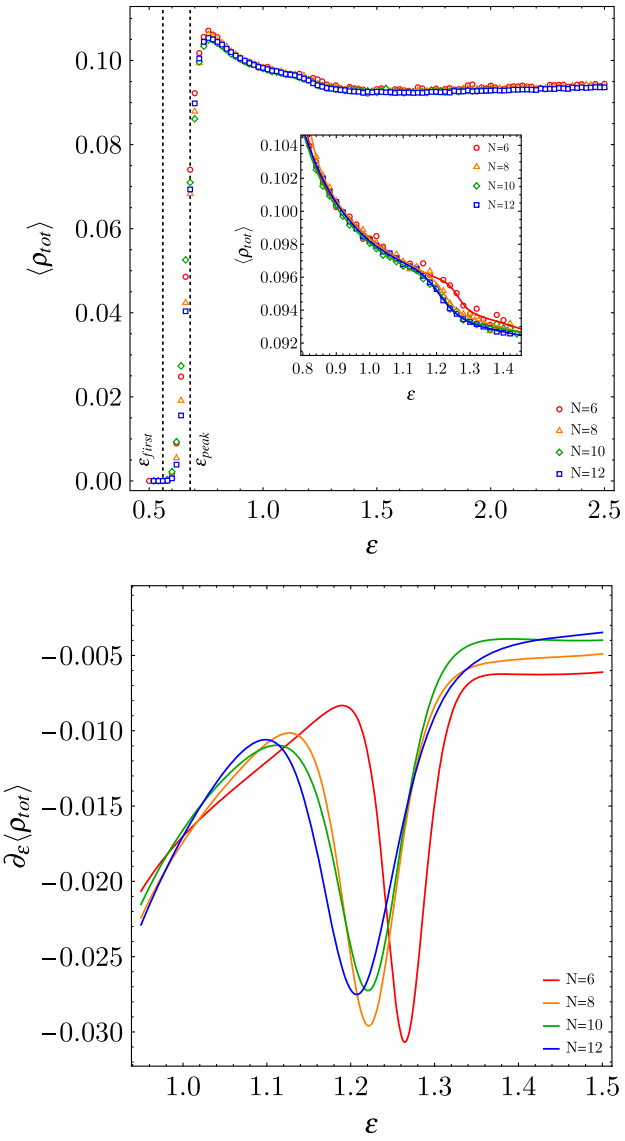

FIG. 21. Density of isolated monopoles vs specific energy for different lattice sizes in 4D U(1) LGT. In the left panel, the monopole density is plotted vs the specific energy of the system for different lattice sizes. The dashed line indicates the specific energy corresponding to monopoles' first appearance ($\varepsilon_{\text{first}} \sim 0.56$) and the energy corresponding to maximum monopole density ($\varepsilon_{\text{peak}} \sim 0.78$). In the inset a detail of the region where micro-canonical phase transition has been identified through MIPA is reported. Both the data derived from numerical simulation (open markers) and the rational fitting function have been reported. In the right panel, the analytical derivative of the fitting function for the density of monopoles has been reported. For both plots, different colors correspond to different lattice sizes: $N = 6$ (red), $N = 8$ (orange), $N = 10$ (green), $N = 12$ (blue).

$$\langle \rho_{\text{tot}} \rangle = \frac{1}{V} \sum_{\boldsymbol{n}} N_{\text{tot}}(\boldsymbol{n}). \tag{G4}$$

1. Analysis of monopoles densities for $N = 12$ and comparison with different lattice sizes

In what follows, the analysis of the density of monopoles as a function of the total energy is reported. In the top panel of Figs. 18, 19, and 20, the density of total density of monopoles, isolated monopoles and pairs are respectively reported for $N = 12$. The energy range for these plots is restricted to those energy where PTs are observed. In the top panel of Figs. 21, 22, and 23, the same densities are respectively reported on the entire range of energies adopted in simulations for different system's size as

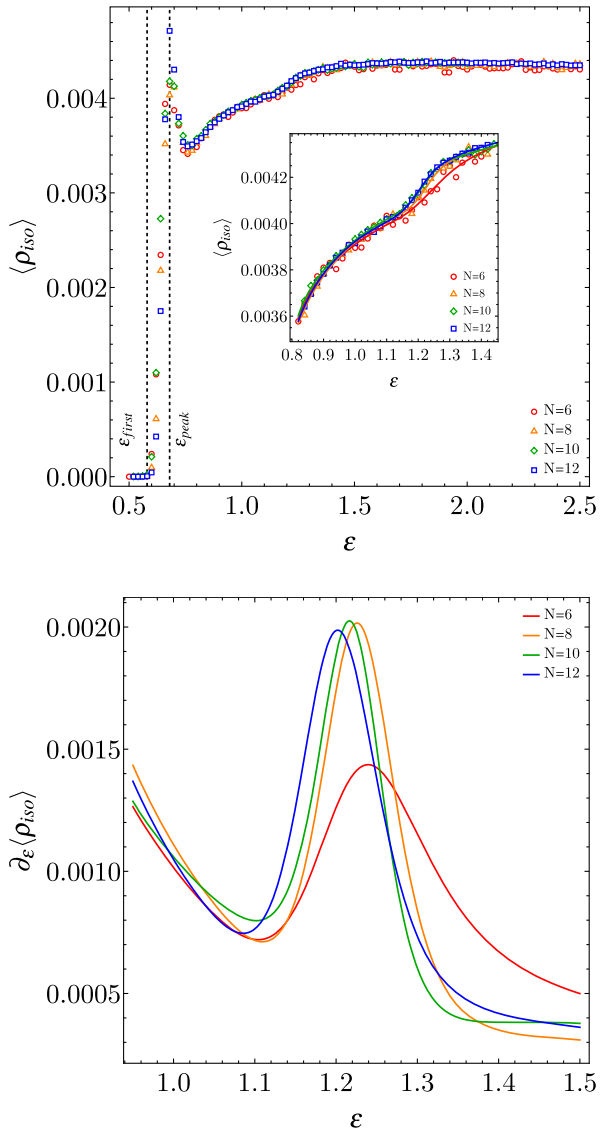

FIG. 22. Density of isolated monopoles vs specific energy for different lattice sizes in 4D U(1) LGT. In the left panel, the density of isolated monopoles is plotted vs the specific energy of the system for different lattice sizes. The dashed line indicates the specific energy corresponding to monopoles' first appearance ($\varepsilon_{\text{first}} \sim 0.56$) and the energy corresponding to a local maximum of isolated monopole density ($\varepsilon_{\text{peak}} \sim 0.78$). In the inset, a detail of the region where microcanonical phase transition has been identified through MIPA is reported. The data derived from numerical simulation (open markers) and the rational fitting function have been reported. In the right panel, the analytical derivative of the fitting function for the density of monopoles has been reported. For both plots, different colors correspond to different lattice sizes: $N = 6$ (red), $N = 8$ (orange), $N = 10$ (green), $N = 12$ (blue).

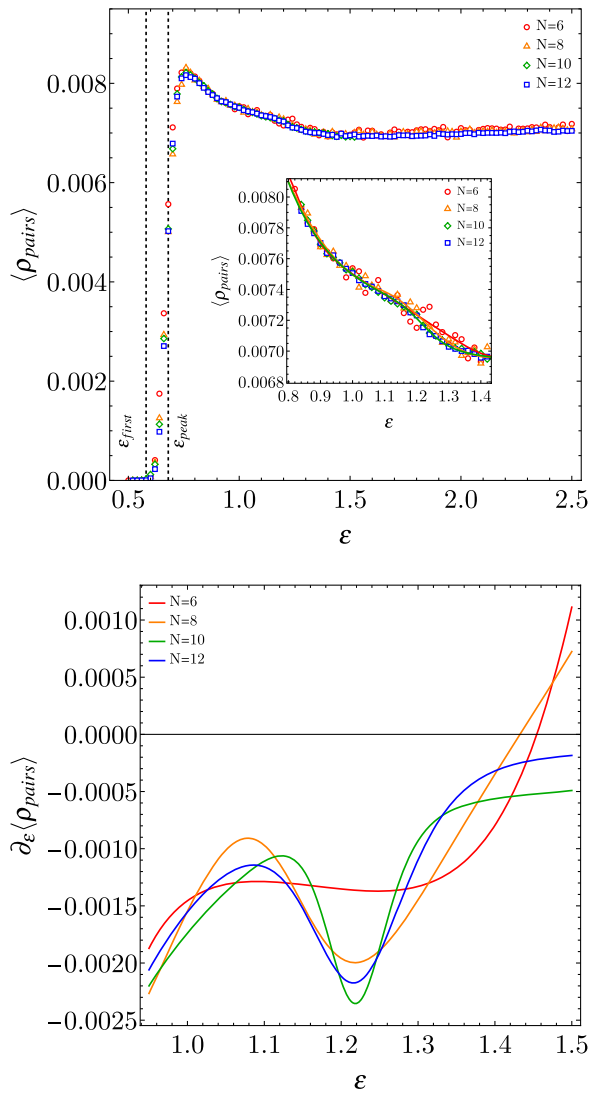

FIG. 23. Density of pairs of monopoles vs specific energy for different lattice sizes in 4D U(1) LGT. In the left panel, the density of pairs of monopoles is plotted vs the specific energy of the system for different lattice sizes. The dashed line indicates the specific energy corresponding to monopoles' first appearance ($\varepsilon_{\text{first}} \sim 0.56$) and the energy corresponding to a maximum density of monopoles pairs ($\varepsilon_{\text{peak}} \sim 0.78$). In the inset, a detail of the region where microcanonical phase transition has been identified through MIPA is reported. The data derived from numerical simulation (open markers) and the rational fitting function have been reported. In the right panel, the analytical derivative of the fitting function for the density of monopole pairs has been reported. For both plots, different colors correspond to different lattice sizes: $N = 6$ (red), $N = 8$ (orange), $N = 10$ (green), $N = 12$ (blue).

specified in the captions. It can be noticed that a consistent part of the monopoles is not isolated nor coupled with other monopoles.

The data on the monopole densities obtained from the numerical simulations are fitted with a rational function of the same form as in Eq. (C4) on the interval $\varepsilon \in [0.86, 2.5]$ to investigate the correlation between the PT identified with MIPA and the dynamics of monopole creation/destruction as a function of the specific energy. In this case, the hyper-parameter has been chosen such that it minimizes the χ^2_{red}.

To validate the fitting procedure, we also calculate the numerical derivatives of monopole densities estimated with finite-difference method from the data estimated from numerical simulation. The energy first-order derivative of the density of total density of monopoles, isolated monopoles and pairs are reported in the bottom panels of Figs. 18, 19, and 20, respectively, for system's size $N = 12$. See the corresponding captions for further details.

Reveals that the first-order derivatives of the isolated monopole density and the density of pairs exhibit a negative-valued minimum (positive-valued maximum) around the critical energy associated to the DPT (see bottom panels in both Figs. 20 and 21). Such an inflection point in monopole density dynamics is located at $\varepsilon_{\mathrm{minDMon}} = 1.202 \pm 0.003$. The value of the energy, $\varepsilon_{\mathrm{maxDMon}} = 1.083 \pm 0.007$ where a negative-valued maximum (positive-valued minimum) in $\partial_\varepsilon \langle \rho_{\mathrm{tot}} \rangle$ and $\partial_\varepsilon \langle \rho_{\mathrm{pairs}} \rangle$ ($\partial_\varepsilon \langle \rho_{\mathrm{iso}} \rangle$) has been observed, is in qualitative agreement with the critical energy corresponding to third-order independent PT.

We will address in future works the problem of reaching a quantitative agreement between the energy values mentioned above. Our experience suggests that a huge computational effort, focused on drastically increasing the statistics in the energy sampling, can help in appreciating the energy behavior of these observables in a quite narrow range.

Finally, the energy, $\varepsilon_{\mathrm{maxD2Mon}} = 1.265 \pm 0.007$, where an inflection point is detected in all the considered monopole densities, corresponds to the critical energy of third-order dependent PT.

APPENDIX H: (NON)EQUIVALENCE OF STATISTICAL ENSEMBLES

In this section, we briefly report and discuss the rigorous results provided by Ellis, Touchette, *et al.* [96] about the (non)equivalence of the ensembles. The underlying idea of their derivation lies in the possibility of defining a mathematical criterion for determining whether the equivalence of the ensembles exists, and it can be summarized as follows. Let us consider the (infinite-size) free energy $F_\infty(\beta) = -\lim_{N\to\infty} \ln Z(\beta, N)$ where Z is the canonical partition function and the (infinite-size) microcanonical entropy, $s_\infty(\varepsilon) = \lim_{N\to\infty} S_N(\varepsilon)/N$. The free energy $F_\infty(\beta)$ can be mathematically defined as the Legendre-Fenchel transform of the microcanonical entropy, and it is denoted with s^*. Thus, we have [7,97]

$$\big(s_\infty(\varepsilon)\big)^* \equiv F_\infty(\beta) \coloneqq \inf_{\varepsilon\in\mathbb{R}} [\beta\varepsilon - s_\infty(\varepsilon)], \tag{H1}$$

whereas the inverse Legendre-Fenchel transform is given by

$$\big(F_\infty(\beta)\big)^* \equiv s_\infty(\varepsilon) \coloneqq \inf_{\beta\in\mathbb{R}} [\beta\varepsilon - F_\infty(\beta)], \tag{H2}$$

where $\varepsilon(= E/N)$ is the specific total energy and β the inverse temperature. The equivalence of ensembles is mathematically defined by the condition [7]

$$F^{**} = s \quad \text{or} \quad s^{**} = F. \tag{H3}$$

Roughly speaking, we can distinguish two cases for which the condition $F^{**} = s$ is satisfied: (i) F_∞ is everywhere differentiable, (ii) s_∞ is everywhere a convex function (in the sense of the supporting line: see the illustration given in Fig. 1 of Ref. [7]). However, in the presence of a first-order PT, at finite-size, $s(\varepsilon)$ admits a nonconvex region (see, for instance, Fig. 1 in Ref. [98]) whereas, in the thermodynamic limit, $s_\infty(\varepsilon)$ admits a degenerate supporting line (limit case of nonconvexity), so it results that $F_\infty(\beta)$ is not differentiable everywhere which is equivalent to saying that $s_\infty(\varepsilon)$, is no longer convex everywhere. In this case, which manifests in the presence of a first-order PT, the equivalence of the canonical and microcanonical ensembles is lost (at least locally).

[1] P. W. Higgs, Phys. Rev. **145**, 1156 (1966).
[2] P. W. Higgs, Phys. Rev. Lett. **13**, 508 (1964).
[3] F. Englert and R. Brout, Phys. Rev. Lett. **13**, 321 (1964).
[4] T. D. Lee, Tsung-Dao, and C. N. Yang, Phys. Rev. **87**, 410 (1952).
[5] C. N. Yang and T. D. Lee, Phys. Rev. **87**, 404 (1952).
[6] D. Ruelle, *Statistical Mechanics: Rigorous Results* (World Scientific, 1999).
[7] H. Touchette, R. S. Ellis, and B. Turkington, Physica (Amsterdam) **340A**, 138 (2004).
[8] R. S. Ellis, K. Haven, and B. Turkington, Nonlinearity **15**, 239 (2002).
[9] H. Touchette and R. S. Ellis, *Nonequivalent Ensembles and Metastability* (World Scientific, 2005).
[10] R. S. Ellis, H. Touchette, and B. Turkington, Physica (Amsterdam) **335A**, 518 (2004).
[11] D. H. E. Gross, *Microcanonical Thermodynamics: Phase Transitions in"Small" Systems* (World Scientific, 2001).
[12] D. H. E. Gross and J. F. Kenney, J. Chem. Phys. **122**, 224111 (2005).
[13] M. Bachmann, *Thermodynamics and Statistical Mechanics of Macromolecular Systems* (Cambridge University Press, 2014).
[14] M. Bachmann, J. Phys. Conf. Ser. **487**, 012013 (2014).

[15] S. Schnabel, D. T Seaton, D. P. Landau, and M. Bachmann, Phys. Rev. E **84**, 011127 (2011).
[16] K. Qi and M. Bachmann, Phys. Rev. Lett. **120**, 180601 (2018).
[17] T. Koci and M. Bachmann, Phys. Rev. E **95**, 032502 (2017).
[18] K. Sitarachu, R. K. P. Zia, and M. Bachmann, J. Stat. Mech. (2020) 073204.
[19] K. Sitarachu and M. Bachmann, J. Phys. Conf. Ser. **1483**, 012009 (2020).
[20] D. Aierken and M. Bachmann, Polymers **12**, 3013 (2020).
[21] K. Qi, B. Liewehr, T. Koci, B. Pattanasiri, M. J. Williams, and M. Bachmann, J. Chem. Phys. **150**, 054904 (2019).
[22] T. Koci and M. Bachmann, Phys. Rev. E **92**, 042142 (2015).
[23] K. Sitarachu and M. Bachmann, Phys. Rev. E **106**, 014134 (2022).
[24] B. Ghofrane, M. Gori, V. Penna, G. Pettini, and R. Franzosi, Entropy **22**, 380 (2020).
[25] G. Pettini, M. Gori, R. Franzosi, C. Clementi, and M. Pettini, Physica (Amsterdam) **516A**, 376 (2019).
[26] L. Di Cairano, J. Phys. A Math. Theor. **55**, 27LT01 (2022).
[27] L. Di Cairano, R. Capelli, B. Ghofrane, and M. Pettini, Phys. Rev. E **106**, 054134 (2022).
[28] L. D. Landau, Zh. Eksp. Teor. Fiz. **7**, 19 (1937).
[29] L. D. Landau, Zh. Eksp. Teor. Fiz. **7**, 627 (1937).
[30] M. Blasone, P. Jizba, and G. Vitiello, *Quantum Field Theory and its Macroscopic Manifestations: Boson Condensation, Ordered Patterns, and Topological Defects* (World Scientific, Singapore, 2011).
[31] H. Umezawa, *Advanced Field Theory: Micro, Macro, and Thermal Physics* (Springer, New York, 1995).
[32] H. J. Rothe, *Lattice Gauge Theories: An Introduction* (World Scientific Publishing Company, Singapore, 2012).
[33] J. Greensite, *An Introduction to the Confinement Problem* (Springer, New York, 2011), Vol. 821.
[34] N. D. Mermin and H. Wagner, Phys. Rev. Lett. **17**, 1133 (1966).
[35] N. D. Mermin, J. Math. Phys. (N.Y.) **8**, 1061 (1967).
[36] S. Elitzur, Phys. Rev. D **12**, 3978 (1975).
[37] J. M. Kosterlitz, J. Phys. C **7**, 1046 (1974).
[38] J. M. Kosterlitz and D. J. Thouless, J. Phys. C **6**, 1181 (1973).
[39] V. L. Berezinskii, Sov. Phys. JETP **32**, 493 (1971).
[40] J. B. Kogut, Rev. Mod. Phys. **55**, 775 (1983).
[41] T. A. DeGrand and D. Toussaint, Phys. Rev. D **22**, 2478 (1980).
[42] J. S. Barber and R. E. Shrock, Nucl. Phys. **B257**, 515 (1985).
[43] J. S. Barber, Phys. Lett. **147B**, 330 (1984).
[44] V. Grösch, K. Jansen, J. Jersak, C. B. Lang, T. Neuhaus, and C. Rebbi, Phys. Rev. **162B**, 171 (1985).
[45] W. Kerler, C. Rebbi, and A. Weber, Phys. Rev. D **50**, 6984 (1994).
[46] J. S. Barber, R. Shrock, and R. Schrader, Phys. Lett. **152B**, 221 (1985).
[47] T. Banks, R. Myerson, and J. B. Kogut, Nucl. Phys. **B129**, 493 (1977).
[48] K. Pyka, J. Keller, H. L. Partner, R. Nigmatullin, T. Burgermeister, D. M. Meier, K. Kuhlmann, A. Retzker, M. B. Plenio, W. H. Zurek, A. Del Campo, and T. E. Mehlstäubler, Nat. Commun. **4**, 2291 (2013).
[49] A. Del Campo and W. H. Zurek, Int. J. Mod. Phys. A **29**, 1430018 (2014).
[50] X. Z. Yu, Y. Onose, N. Kanazawa, J. H. Park, J. H. Han, Y. Matsui, N. Nagaosa, and Y. Tokura, Nature (London) **465**, 901 (2010).
[51] S. Heinze, K. Von Bergmann, M. Menzel, J. Brede, A. Kubetzka, R. Wiesendanger, G. Bihlmayer, and S. Blügel, Nat. Phys. **7**, 713 (2011).
[52] T. W. B. Kibble, J. Phys. A Math. Gen. **9**, 1387 (1976).
[53] G. F. Nataf, M. Guennou, J. M. Gregg, D. Meier, J. Hlinka, E. K. H. Salje, and J. Kreisel, Nat. Rev. Phys. **2**, 634 (2020).
[54] X. Wang, D. S. Miller, E. Bukusoglu, J. J. De Pablo, and N. L. Abbott, Nat. Mater. **15**, 106 (2016).
[55] D. J. E. Callaway and A. Rahman, Phys. Rev. Lett. **49**, 613 (1982).
[56] D. J. E. Callaway and A. Rahman, Phys. Rev. D **28**, 1506 (1983).
[57] D. J. E. Callaway, Contemp. Phys. **26**, 23 (1985).
[58] D. J. E. Callaway, Contemp. Phys. **26**, 95 (1985).
[59] T. D. Andersen, Phys. Rev. D **99**, 016012 (2019).
[60] J. B. Kogut, J. Polonyi, H. W. Wyld, J. Shigemitsu, and D. K. Sinclair, Nucl. Phys. **B251**, 311 (1985).
[61] J. Polonyi and H. W. Wyld, Phys. Rev. Lett. **51**, 2257 (1983).
[62] J. Jersák and T. Neuhaus, and P. M. Zerwas, Phys. Lett. **133B**, 103 (1983).
[63] S. Sarkar, Sci. Rep. **11**, 1 (2021).
[64] B. Lautrup and M. Nauenberg, Phys. Lett. **95B**, 63 (1980).
[65] D. R. Stump and J. H. Hetherington, Phys. Lett. B **188**, 359 (1987).
[66] H. G. Evertz, T. Jersak, T. Neuhaus, and P. M. Zerwas, Nucl. Phys. **B251**, 279 (1985).
[67] K. G. Wilson, Phys. Rev. D **10**, 2445 (1974).
[68] S. Duane, Nucl. Phys. **257**, 652 (1985).
[69] E. M. Pearson, T. Halicioglu, and W. A. Tiller, Phys. Rev. A **32**, 3030 (1985).
[70] M. Creutz, L. Jacobs, and C. Rebbi, Phys. Rev. D **20**, 1915 (1979).
[71] G. Bhanot, Phys. Rev. D **24**, 461 (1981).
[72] K. J. M Moriarty, Phys. Rev. D **25**, 2185 (1982).
[73] M. Creutz, L. Jacobs, and C. Rebbi, Phys. Rep. **95**, 201 (1983).
[74] T. A. DeGrand and D. Toussaint, Phys. Rev. D **24**, 466 (1981).
[75] D. G. Caldi, Nucl. Phys. **B220**, 48 (1983).
[76] J. Tobochnik and G. V. Chester, Phys. Rev. B **20**, 3761 (1979).
[77] J. B. Kogut and E. Dagotto, Phys. Rev. Lett. **59**, 617 (1987).
[78] S. Duane, A. D. Kennedy, B. J. Pendleton, and D. Roweth, Phys. Lett. B **195**, 216 (1987).
[79] J. B. Kogut, Rev. Mod. Phys. **51**, 659 (1979).
[80] M. G. Vasin and V. M. Vinokur, Physica (Amsterdam) **525A**, 1161 (2019).
[81] M. G. Vasin, Phys. Rev. E **106**, 044124 (2022).
[82] L. Balents, Nature (London) **464**, 199 (2010).

[83] L. Savary and L. Balents, Rep. Prog. Phys. **80**, 016502 (2016).
[84] H. Aoki, T. Sakakibara, K. Matsuhira, and Z. Hiroi, J. Phys. Soc. Jpn. **73**, 2851 (2004).
[85] R. Higashinaka, H. Fukazawa, K. Deguchi, and Y. Maeno, J. Phys. Soc. Jpn. **73**, 2845 (2004).
[86] A. Farhan, M. Saccone, C. F. Petersen, S. Dhuey, R. V. Chopdekar, Y. L. Huang, N. Kent, Z. Chen, M. J. Alava, T. Lippert, A. Scholl, and S. van Dijken, Sci. Adv. **5**, eaav6380 (2019).
[87] S. H. Skjærvø, C. H. Marrows, R. L. Stamps, and L. J. Heyderman, Nat. Rev. Phys. **2**, 12 (2020).
[88] C. Castelnovo, M. Roderich, and L. S. Shivaji, Nature (London) **451**, 42 (2008).
[89] M. N. Chernodub, V. A. Goy, and A. V. Molochkov, and A. S. Tanashkin, Phys. Rev. D **105**, 114506 (2022).
[90] M. N. Chernodub, V. A. Goy, and A. V. Molochkov, Phys. Rev. D **95**, 074511 (2017).
[91] M. N. Chernodub, V. A. Goy, A. V. Molochkov, and H. H. Nguyen, Phys. Rev. Lett. **121**, 191601 (2018).
[92] M. N. Chernodub, V. A. Goy, and A. V. Molochkov, Phys. Rev. D **96**, 094507 (2017).
[93] S. Varrette, P. Bouvry, H. Cartiaux, and F. Georgatos, Management of an academic HPC cluster: The UL experience, in *Proceedings of the 2014 International Conference on High Performance Computing & Simulation (HPCS 2014)* (IEEE, Bologna, Italy, 2014), pp. 959–967.
[94] hpc.uni.lu
[95] L. Casetti, Phys. Scr. **51**, 29 (1995).
[96] R. S. Ellis, K. Haven, and B. Turkington, J. Stat. Phys. **101**, 999 (2000).
[97] H. Touchette, Legendre-Fenchel transforms in a nutshell (2005), https://appliedmaths.sun.ac.za/htouchette/archive/notes/lfth2.pdf.
[98] A. Hüller, Z. Phys. B Condens Matter **95**, 63 (1994).